1 Climatology and Interannual Variability of Quasi-Global Intense Precipitation Using

2 Satellite Observations

3

4

5 Martina Ricko,[a] Robert F. Adler,[b] and George J. Huffman[c]

6

7

8 *Journal of Climate*

9

13

14 _____

15 *Corresponding author*: Martina Ricko, SGT Inc., 7701 Greenbelt Rd., Suite 400,

16 Greenbelt, MD 20770. E-mail: mricko@sgt-inc.com

17

18 [a]SGT Inc., Greenbelt, Maryland

19 [b]Earth System Science Interdisciplinary Center, University of Maryland, College Park,

20 College Park, Maryland

21 [c]NASA Goddard Space Flight Center, Greenbelt, Maryland

22   **Abstract**

23   Climatology and variations of recent mean and intense precipitation over a near global

24   (50°S-50°N) domain on a monthly and annual time scale are analyzed. Data used to

25   derive daily precipitation to examine the effects of spatial and temporal coverage of

26   intense precipitation are the current Tropical Rainfall Measuring Mission (TRMM)

27   Multi-satellite Precipitation Analysis (TMPA) 3B42 Version 7 precipitation product, with

28   high spatial and temporal resolution during 1998-2013. Intense precipitation is defined by

29   several different parameters, such as a 95th percentile threshold of daily precipitation, a

30   mean precipitation that exceeds that percentile or a fixed threshold of daily precipitation

31   value (e.g., 25 and 50 mm day^{-1}). All parameters are used to identify the main

32   characteristics of spatial and temporal variation of intense precipitation. High correlations

33   between examined parameters are observed, especially between climatological monthly

34   mean precipitation and intense precipitation, both over tropical land and ocean. Among

35   the various parameters examined, the one best characterizing intense rainfall is a fraction

36   of daily precipitation $\geq$25 mm day^{-1}, defined as a ratio between the intense precipitation

37   above used threshold and mean precipitation. Regions that experience an increase in

38   mean precipitation likely experience a similar increase in intense precipitation, especially

39   during the El Niño-Southern Oscillation (ENSO) events. Improved knowledge of this

40   intense precipitation regime and its strong connection to mean precipitation given by the

41   fraction parameter can be used for monitoring of intense rainfall and its intensity on a

42   global to regional scale.

1. Introduction

Extreme climatic events frequently occur over areas that experience anomalous precipitation regimes on several time scales. Flooding and landslides are good examples of natural hazard events that are highly connected to excessive precipitation on a daily scale (e.g., Wu et al. 2012; Kirschbaum et al. 2012). On a longer time scale, from months to seasons, anomalous lack of precipitation causes drought events producing substantial impacts on agriculture, ecosystems and society, directly affecting water resources, hydroelectric power, and changes of affected areas. Our concerns are more frequently about those natural events that cause huge economic and human losses on a daily scale. Therefore, promptness, regularity and accuracy in predicting these disastrous events (such as flooding and landslides) need constant focus and further improvement in order to minimize damage from these events.

Numerous studies have investigated the changes in intensity, frequency and trends, with causes and importance of these events. Cavalcanti (2012) showed that large-scale features and synoptic weather systems mainly cause heavy precipitation producing flooding in certain regions, over tropical and extratropical areas. A systematic increase in intensity and frequency of heavy precipitation events in tropical and subtropical regions have been clearly evidenced, and observed changes have been shown to be consistent with most climate model projections (e.g., Allan and Soden 2008; Min et al. 2011; Shiu et al. 2012). Even though precipitation extremes are expected to increase in the future over large parts of the globe as global climate warms (Easterling et al. 2000; Kharin et al. 2007; O'Gorman 2012), with higher moisture content being available to form intense precipitation events and provide additional energy to further intensify such events, we

66 still don't know how strong a relationship between the mean state of precipitation and

67 intense precipitation frequency is on the most recent climate scale.

68   Intensity of precipitation events is projected to increase over areas that experience

69 increases in mean precipitation. A direct link between the mean and intense precipitation

70 (i.e., 95th percentile) has already been confirmed in rain-gauge observations and model

71 predictions both in space and time prior 2000 (e.g., Benestad et al. 2012). However, the

72 increases in intense precipitation derived by different model simulations are shown to be

73 higher than those expected in mean precipitation in most tropical and high-latitude areas

74 (e.g., Trenberth et al. 2003; Held and Soden 2006; Kharin et al. 2007). On the opposite

75 side, there is a tendency for drying of the mid-continental areas during warm periods,

76 resulting in greater risk of droughts in those regions. With current climate change, and

77 especially global warming, Lau et al. (2013) provided evidence that both intense

78 precipitation and drought events may increase, indicating most increases in heavy

79 precipitation over wet regions of the tropical zones around the equator, particularly in the

80 Pacific Ocean and Asian monsoon regions. Similarly, arid land areas outside the tropics

81 and regions with moderate precipitation could become drier (Dai 2011). A clear

82 connection between global mean temperature and both mean and intense precipitation on

83 a large-scale spatial domain and a long time scale (1945-1995) has been found by

84 Benestad (2013), indicating a number of useful climate applications.

85   Lau and Wu (2011) have investigated the climatology and changes in precipitation

86 over tropical oceans, however, using a shorter record of the Tropical Rainfall Measuring

87 Mission (TRMM) data (1998-2009). They showed that intense (95th percentile)

88 precipitation is associated with the Intertropical Convergence Zone (ITCZ), South Pacific

89   Convergence Zone (SPCZ) and summer monsoon regions, and experiences large increase

90   coupled to a reduction in light to moderate rain over warmer ocean regions with

91   increasing sea surface temperature (SST). They also found that intense precipitation

92   events are most sensitive to changes in tropical mean SST, and that increases of 80–90%

93   of the most extreme intense rain (the top 5%) per degree SST rise can be expected. In

94   addition, Liu and Allan (2012) have also investigated precipitation extremes in multi-

95   satellite data, and have confirmed a strong positive response of the tropical ocean

96   precipitation to changes in temperature due to El Niño-Southern Oscillation (ENSO)

97   events. It has also been shown that, even over land, extreme precipitation events are more

98   sensitive to climate variability, such as ENSO, than monthly or seasonal total rainfall, and

99   that the frequency of extreme events experiences a larger and spatially more extensive

100   significant increase than these totals, with reduction of light to moderate rain (Grimm and

101   Tedeschi 2009).

102   In order to develop high-resolution regional climate scenarios for climate change

103   impact studies, including global warming, and to investigate ENSO's natural variability,

104   it is necessary first to analyze longer high-resolution climatic precipitation data sets

105   focusing on intense precipitation on a regional to global scale. Unfortunately, large

106   periods of unavailable and poor quality observational data still limit such analysis,

107   together with low representativeness of *in situ* observations. Most previous studies

108   detecting the increased frequency of intense precipitation events in tropical and

109   subtropical regions have used either *in situ* data over land or long-term monthly satellite

110   precipitation data. However, both types of data do not have sufficient spatial coverage

111   and temporal homogeneity to analyze the intense precipitation events in detail.

112   Furthermore, local changes in precipitation and its extremes are highly variable, and

113   highly dependent upon small shifts in the large-scale atmospheric circulation and regional

114   feedbacks that current climate models still cannot simulate correctly. Consequently,

115   current knowledge of changes in the occurrence of global intense precipitation is still

116   quite limited.

117   In this study, we utilize a 16-year record of daily precipitation derived from a uniform

118   high resolution (3-hr temporal and 0.25° grid spatial) Tropical Rainfall Measuring

119   Mission (TRMM) Multi-satellite Precipitation Analysis (TMPA) Version 7 satellite

120   precipitation data over a near-global domain (50°N-50°S), to analyze climatological

121   intense precipitation over land and ocean during the period 1998-2013. The emphasis

122   here is on the climatology of "intense" precipitation, but we will also give parameters

123   such as mean precipitation, fraction of daily precipitation, and conditional daily

124   precipitation rate, to provide a climatological context. For this study, we consider

125   "extreme" precipitation to be only precipitation amount above the 99th percentile

126   threshold, but this parameter is not the focus of this study. Rather, we explore the use of

127   various measures of intense precipitation, including high percentile thresholds (e.g., 95th

128   percentile), mean precipitation above that percentile, number of days in a month above

129   some daily fixed thresholds (e.g., 25 and 50 mm day^{-1}), and mean precipitation above

130   those daily thresholds in a month. Consequently, the parameter that best describes a

131   relationship between the mean precipitation and intense precipitation is analyzed, and can

132   then be easily adopted globally and/or regionally to investigate regions that experience

133   natural hazard events, such as floods and landslides, as has already been done in a

134   preliminary fashion for landslides (Kirschbaum et al. 2012).

135   In addition, we investigate spatial and temporal variations of intense precipitation in

136   relation to its natural variability (i.e., ENSO events), rather than to climate change.

137   Several previous studies (e.g., Curtis et al. 2007; Grimm and Tedeschi 2009; Lau and Wu

138   2011) have already analyzed the ENSO influence on intense precipitation mostly over

139   land and Dai et al. (1997) have found that ENSO is the single largest cause of global

140   intense precipitation over land.

141   The objectives of this study are: (1) to define the best parameter that will help

142   establish the pattern and characteristics of climatology of intense precipitation events, and

143   (2) to understand inter-annual variations of monthly mean and intense precipitation

144   relating them to large-scale climate variability (e.g., ENSO), using recent uniform

145   satellite data over land and ocean over the tropical and sub-tropical domain. The

146   remainder of this paper is organized as follows. Section 2 describes the data products

147   used. Definitions for intense precipitation and analysis procedure are explained in section

148   3. Spatial patterns of intense precipitation climatology are explained in section 4. The

149   results of the intense precipitation characteristics, both over land and ocean, and during

150   El Niño and La Niña periods, are described and examined in section 5. Discussion and

151   conclusions are presented in section 6.

152   **2. Data**

153   In this study, we utilize the Version 7 TMPA satellite precipitation product (TMPA

154   3B42 V7; Huffman et al. 2007, 2010), which provides near-global coverage (50°N-50°S)

155   at 3-hourly, 0.25° resolution. The TMPA precipitation estimates are a combination of

156   different space-borne sensors, including radar and passive microwave, infrared data, and

157   gauge measurements. Several important changes are included in the TMPA V7 data

158 products: (1) additional satellite data, including the early part of the Microwave Humidity

159 Sounder (MHS) record, the entire operational Special Sensor Microwave Imager/Sounder

160 (SSMIS) record; (2) a new infrared (IR) brightness temperature data set from

161 geosynchronous satellites for the period before the start of the Climate Prediction Center

162 (CPC) 4-km Merged Global IR data set (January 1998–February 2000) with the National

163 Climatic Data Center (NCDC) GridSat-B1 spatial resolution finer than the TMPA 0.25°

164 resolution and full coverage of the TRMM domain; (3) uniformly reprocessed input data

165 from several additional sources: the Advanced Microwave Sounding Unit-B (AMSU-B),

166 MHS, TRMM Combined Instrument (TCI), TRMM Microwave Imager (TMI), the

167 Special Sensor Microwave/Imager (SSM/I), and the Advanced Microwave Scanning

168 Radiometer-Earth Observing System (AMSR-E); and (4) adjustment by the Global

169 Precipitation Climatology Centre (GPCC) monthly surface precipitation gauge analysis

170 (Schneider et al. 2011). An additional retrospective processing for the TMPA V7 data

171 series had to be carried out when processing issues were discovered omitting the AMSU

172 microwave precipitation data during 2000-2010 in the first retrospective processing

173 (Huffman and Bolvin 2012).

174 Several recent studies have addressed the uncertainty of high-resolution global

175 satellite precipitation products, showing their performance depending on the precipitation

176 regime, being more accurate during summer times and at lower latitudes (Arkin et al.

177 2008; Ebert et al. 2007). For daily bias and precipitation frequency, Ebert et al. (2007)

178 showed that the Infra-Red/Passive Microwave merged satellite precipitation estimates are

179 almost as good as those from ground-based radar over the United States. In addition,

180 Sapiano and Arkin (2009) performed an inter-comparison between several high-

181   resolution global satellite products with gauge data, and showed good performance of

182   satellite precipitation data but with relatively high biases (except for gauge-adjusted

183   products over land).

184   Su et al. (2008) evaluated an earlier Version 6 (V6) of the TMPA 3B42 precipitation

185   data set using rain gauge data on various temporal and spatial scales. Good qualitative

186   agreement was found between the TMPA and gauge data in the occurrence of

187   precipitation events, but an overestimation of most high precipitation events on a daily

188   scale over the La Plata basin in South America was observed with noticeable regional

189   variation of the TMPA performance. On a daily scale over the contiguous United States,

190   a study by Tian et al. (2009) showed a comparison of six different high-resolution

191   satellite-based precipitation data sets (including the TMPA 3B42 V6 and TMPA 3B42

192   RT) against the gauge data. Overall, all precipitation data sets showed overestimation of

193   strong precipitation (>40 mm day^{-1}) in summer and underestimation in winter, by as

194   much as 50%, and missing a significant amount of light precipitation

195   (<10 mm day^{-1}) up to 40%. Consistently missed precipitation in winter was mainly

196   observed over mountainous regions, such as the Rockies, and the northeastern U.S.,

197   confirming a common challenge to all satellite data sets. In addition, Scheel et al. (2011)

198   confirmed that the same TMPA 3B42 V6 estimates in the Central Andes are significantly

199   better on a monthly scale, but overestimation of heavy precipitation still exists.

200   Therefore, we examine here the latest TMPA 3B42 V7 precipitation data set and its

201   performance in the occurrence of heavy rainfall events (i.e., climatological intense

202   precipitation).

203   **3. Methodology and definitions**

204   We compute a daily precipitation data set from 3-hourly TMPA 3B42 V7 for the

205   period of 1998-2013, keeping the original 0.25° spatial resolution. This daily

206   precipitation data set is used to compute monthly statistics over a 16-year climatology of

207   various parameters related to mean and heavy precipitation on a monthly and annual time

208   scale. To set the context of the discussion, we use the total daily precipitation value (R) at

209   each grid point to calculate the mean monthly value of daily precipitation for each month

210   in the year, for the 1998-2013 period (R_{mean}, in mm day^{-1}). We also compute the

211   conditional precipitation rate for the month (i.e., the mean precipitation rate for days with

212   R >0 mm day^{-1}; R_{cond}, in mm day^{-1}) and the fraction of daily precipitation for days in the

213   month with R >0 mm day^{-1} (F_0). These three parameters are related (i.e., $R_{mean}=F_0 \cdot R_{cond}$).

214   For examining intense daily precipitation, we explored a number of statistical

215   parameters to determine monthly values useful for spatial and temporal comparison. Our

216   definitions of these parameters follow closely, but not exactly, those of the Expert Team

217   on Climate Change Detection and Indices (ETCCDI, Karl et al. 1999; Peterson et al.

218   2001). We have specifically examined parameters such as percentiles near the high end of

219   the precipitation distribution, frequency (number of days) above a threshold, and

220   precipitation amounts over certain thresholds. This has been done to attempt to find

221   statistics that would be useful for description of climatology and variations on a monthly

222   scale, and for possible use and links to natural hazards, such as floods and landslides over

223   land, and tropical cyclones and other phenomena over ocean.

224   Since we have a data set with a limited number of years; in terms of percentiles, we

225   have stayed with a relatively conservative value to characterize "intense" daily rainfall

226   (i.e., the 95th percentile). We calculated the 95th percentile of daily precipitation (R_{95p}, in

227   mm day^{-1}), and the mean precipitation in a month above this daily threshold (R_{95}, in mm

228   day^{-1}). In addition, we have calculated the number of days in a month with daily

229   precipitation above fixed threshold values (R $\geq$25, 50 and 75 mm day^{-1}; N_{25}, N_{50}, N_{75}),

230   and the intense precipitation above the same daily thresholds (R_{25}, R_{50}, in mm day^{-1}). The

231   fraction of intense precipitation is calculated for all examined thresholds as well (F_{95}, F_{25},

232   F_{50}), balancing their corresponding intense precipitation amounts (R_{95}, R_{25}, R_{50}) with the

233   mean precipitation (e.g., $F_{95}=R_{95}/R_{mean}$). Results from examining these different statistical

234   parameters allowed us to focus on just a few of them when we moved onto the relations

235   between variables and their inter-annual variations. Table 1 summarizes the definitions

236   and units for all statistical parameters we use to explain climatology of mean and intense

237   precipitation.

238   **4. Climatology of monthly mean precipitation**

239   There are few high quality global or quasi-global climatologies of precipitation that

240   span both land and ocean. The relatively recent TRMM data (1998-present) has resulted

241   in significant new knowledge regarding rainfall system structure and other attributes

242   across the tropics and also a rainfall climatology, the TRMM Composite Climatology

243   (TCC) (Adler et al. 2009; Wang et al. 2014), based on information from both the TRMM

244   Precipitation Radar (PR) and the satellite's passive microwave sensor, the TRMM

245   Microwave Imager (TMI). The Global Precipitation Climatology Project (GPCP)

246   monthly product (Adler et al. 2003; Huffman et al. 2009) is a widely used analysis at 2.5°

247   latitude-longitude resolution covering a time period over 30 years. Even though there

248   exists a GPCP daily product (Huffman et al. 2001), for a similar time span as the TMPA,

249   the TMPA has a higher spatial resolution (0.25°) and is considered of higher quality due

250   to the greater amount of microwave-based rainfall estimates in it. The absolute

251   magnitudes of estimated mean precipitation over ocean are probably best estimated by

252   the GPCP and TCC, which have very similar ocean totals, but with some relatively small

253   regional differences. The TMPA may be overestimating mean values over the ocean

254   somewhat (~8%) due to processing and calibration issues (Huffman and Bolvin 2012).

255   However, this issue does not detract significantly from the search for information on the

256   time and space scales of this study. The mean precipitation values over land in the TMPA

257   are also not impacted by this issue.

258   The annual, January, and July means of daily rainfall (R_{mean}) are shown in Fig. 1. The

259   annual climatology map shows very clear features of the Inter-Tropical Convergence

260   Zone (ITCZ) across both the Pacific and Atlantic Oceans, with a not-as-narrow extension

261   through the Maritime Continent into the Indian Ocean. In the Atlantic and Pacific

262   Oceans, the axis of the annual maximum is just north of the equator, while in the Indian

263   Ocean axis falls south of that marker. A northwest-southeast extension of the ITCZ in the

264   South Pacific Ocean, called the South Pacific Convergence Zone (SPCZ), is another

265   feature with the maximum values of mean rainfall. Over tropical land, most striking

266   features with significant rainfall are located over the equatorial African and South

267   American regions. At higher latitudes, two characteristic precipitation bands associated

268   with extensions of ocean currents (the Gulf Stream in the North Atlantic Ocean and

269   Kuroshio in the North Pacific Ocean) are observed along the east coasts of North

270   American and Asian continent, both with significant annual rainfall amounts. The

271   January and July maps show the distinct shift of the seasonal rains with migration of the

272   sun over the tropics, with a larger shift over land than over water describing the

273   monsoons. Enlarged heavy rainfall areas in January are observed in the equatorial

274   Atlantic and the western Pacific, especially over the SPCZ, coastal Southeast Asian

275   region, western extension of the South Equatorial Current in the Southwestern Indian

276   Ocean, and east and north of Madagascar. At mid-latitudes, the rain bands associated

277   with the Gulf Stream and Kuroshio currents are enlarged and extended towards the

278   central and eastern parts of the oceans. Over the land, a shift of maximum rainfall

279   towards the south of the equator in Africa, South America and northern Australia is

280   clearly observed. A coastal region with significant rain is also found in the tropical and

281   subtropical South America, over the northern, southeastern and southern coast of Brazil

282   (including the eastern parts of the Rio de La Plata basin), and over the South Atlantic

283   Ocean along the Brazilian coast. In July, a strong shift of maximum rainfall towards the

284   north of the equator is observed in the ITCZ and SPCZ regions in the Pacific and Atlantic

285   Oceans. Over land, heavy rain regions are found north of the equator in Africa, Central

286   and South America, and near the Asian mountainous regions (i.e., the Tibetan Plateau)

287   where orographic effect enhances the total rainfall amount. In addition, at higher

288   latitudes, northeastern Asian land and coastal regions experience higher rainfall during

289   the Northern Hemisphere summer months. Bands of enhanced rainfall from storm tracks

290   over the Southern Hemisphere mid-latitudes of the Pacific and Atlantic Oceans are

291   observed as well. Overall, we can observe higher maximum values with smaller spatial

292   coverage of rainfall in July than in January.

293   **5. Climatology of fraction of days with precipitation**

294   Figure 2 displays maps of the fraction of days with rain >0 mm day^{-1} (F_0). This

295   fraction (F_0) multiplied by the conditional precipitation rate (R_{cond}, Fig. 3) is equal to the

296   mean precipitation value (R_{mean}, Fig. 1), that is, $F_0 = R_{mean}/R_{cond}$, and describes how often

297   it precipitates, irrespective of the amount. The main precipitation areas are clearly

298   evident, as expected, with very high fractions (>0.7) in the annual map along the ITCZ

299   over both ocean and land, with secondary maxima averaging ~0.6 over the middle

300   latitude oceans, especially over the Northern Hemisphere. When examining the maps of

301   monthly climatologies (shown here just January and July, Fig. 2), the fractional days of

302   precipitation (F_0) over the higher latitude oceans are now roughly equivalent of those in

303   the tropics, especially during the Northern Hemisphere winter. For example, in January

304   the value of F_0 over the Pacific and Atlantic Oceans at about 30°N is the same as the F_0

305   values over the deep tropics (between 0.7-0.9). Therefore, at these higher latitude

306   locations, as expected, precipitation is as frequent as in the tropical belt maxima, but the

307   intensity on average is lower.

308   The conditional precipitation rate (R_{cond}), or how hard it is precipitating when

309   precipitation is occurring, is a first measure of intensity in this study. As seen in Fig. 3,

310   R_{cond} has a different geographic distribution than the two previous parameters. Even on

311   the annual map, R_{cond} maxima appear in locations where they were absent or muted in the

312   R_{mean} and F_0 maps, including eastern China, eastern North America, southeastern South

313   America and other smaller areas over land. In the seasonal maps, during the Northern

314   Hemisphere winter (January) higher values of R_{cond} (>14 mm day^{-1}) are observed mostly

315   over the tropical Southern Hemisphere (5°N-25°S), including most of the South

316   American land, northern Australia, Indonesia and parts of southeast African land, and

317   over ocean the SPCZ and the Indian Ocean area. In mid-latitudes, eastern parts of North

318   American land and Euro-Asian land with eastern China experience higher values of R_{cond}

(even >16 mm day^{-1}). A northward shift of high values is observed during the Southern

Hemisphere winter (July), when land (20°N-0°) experiences extremely high values of

R_{cond} over most of Southeast Asia, including India, Indonesia, Central America, northern

South America and the La Plata basin, and northern tropical Africa; while maximum

values of R_{cond} over ocean are observed in most of the ITCZ and in particular over the

Gulf Stream region. Over the monsoon areas of Asia and Australia, one can easily see the

monsoon associated with intense rainfall events switching back and forth between the

hemispheres, from January to July (Fig. 3b-c). In January, the features over eastern China

and the U.S. are associated with winter cyclone events. Perhaps the most interesting

features are over South America, where a large area of high values exists in January from

the Amazon southward, while in July (local winter) two maxima in R_{cond} exist over the

northern Amazon and the southeastern coast (the La Plata basin). A maximum point

value of the highest conditional mean precipitation rate in the tropical region is observed

to be 44 mm day^{-1} in January over the southern Philippines and 53 mm day^{-1} in July over

the Meghalaya mountains and west coast of India, with 30 mm day^{-1} in the annual mean

observed over the western coast of Colombia (Fig. 3). The month with the lowest

maximum value of R_{cond} is April (35 mm day^{-1} over the northern Arabian Sea), while

February surprisingly reaches the highest maximum point value of 122 mm day^{-1} over

some eastern parts of Ethiopia due to a second rainy season lasting until the end of

February (figures not shown).

6. **Climatology of intense rainfall**

As described in the previous section, many previous studies (e.g., Gu et al. 2007;

Adler et al. 2008; Huffman et al. 2009; Lau and Wu 2011) have been devoted to

342   characterize climatological features of mean precipitation, along with their patterns and

343   variability. Here focus is more on daily intense precipitation events, their means, patterns,

344   anomalies, and variations, using the best currently available consistent high-resolution

345   multi-satellite TMPA precipitation data set. A number of parameters related to intense

346   daily precipitation are examined, keeping in mind the relatively short duration of the data

347   set (16 years, 1998-2013).

348   *6.1. 95th percentile of precipitation*

349   The first set of intense precipitation variables we examine is related to the 95th

350   percentile of precipitation. That particular percentile was chosen instead of, for example,

351   the 99th percentile, to give a good measure of intense precipitation events, but also to

352   avoid producing a very noisy field at the higher percentile due to a relatively short data

353   record. One goal of examining these measures of intense precipitation on a daily scale is

354   to understand how they relate to each other, and which ones are the best parameters to

355   focus on, especially in relation to hazardous impacts (e.g., floods and landslides).

356   The distribution of the 95th percentile value (R_{95p}) is shown in Fig. 4. This parameter

357   is defined as a daily precipitation rate threshold (including zero values, in mm day^{-1}) in a

358   month at a grid point, below which 95% of the daily rainfall amounts occur, so 5% of all

359   the days have rainfall amounts greater than this value. For example, for months with 30

360   days in a month, the days with precipitation $\geq$95th percentile are 1.5 days, meaning R_{95p}

361   contribution is from the heaviest rainfall of 1 or 2 days. The characteristic pattern of R_{95p}

362   follows that of R_{mean} and F_0 in the annual mean, with the typical features of the

363   atmospheric general circulation over the tropics: the ITCZ, SPCZ, and enhanced rainfall

364   over the Maritime Continent (Southeast Asia), northern tropical Africa, and Central and

365 northern South America; with a strong north-south precipitation gradient. Maximum

366 values observed in R_{mean} are in the range of 10-20 mm day^{-1} (with an absolute maximum

367 of 24 mm day^{-1}; Fig. 1a), while R_{95p} gives much higher values (up to 104 mm day^{-1}; Fig.

368 4a), as expected.

369   Representative months of two contrasting seasons, January and July, are chosen for

370 analysis of opposite regimes of intense monthly mean precipitation, addressing its

371 seasonal variation (Fig. 4b-c). A north-south migration of the ITCZ is clearly observed

372 where maximum precipitation regions reside, especially over land. A strong maximum of

373 R_{95p} (up to 47 mm day^{-1}) during July is also observed over the eastern parts of the Rio de

374 la Plata basin, located in south-central South America (La Plata hereafter), with a

375 seasonal shift northwards in January (Fig. 4b-c). A maximum value of mean precipitation

376 over the tropics is 27 mm day^{-1} in January and 43 mm day^{-1} in July (Fig. 1b-c), while R_{95p}

377 has a maximum value of 142 mm day^{-1} in January and 190 mm day^{-1} in July (Fig. 4b-c),

378 clearly indicating the wettest period in the tropics during boreal summer. The month with

379 the lowest maximum value of R_{mean} over the tropics is April, with a maximum of 22 mm

380 day^{-1}, while R_{95p} reaches maximum of 102 mm day^{-1} (figures not shown).

381   The only areas that are wetter during the boreal winter season than the rest of the year

382 are the westerly storm tracks regions over the Pacific and Atlantic Oceans in mid-

383 latitudes, with the maximum R_{mean} of 8-11 mm day^{-1} (Fig. 1b) and the maximum R_{95p} of

384 30-50 mm day^{-1} (Fig. 4b). Despite the fact that seasonal variability of precipitation is

385 more pronounced outside of the tropics, where rainy seasons differ much more

386 regionally, we focus on the intense precipitation variability more in the tropical and less

387 in the extra-tropical regions due to the data availability and quality in this region.

Even though we are looking at only 16 years of precipitation data, there are some significant differentiating spatial features between mean and intense precipitation that are worth mentioning. In comparison, regions with high intense precipitation (i.e., R_{95p}) are significantly larger in area than those characterized by mean precipitation (R_{mean}) over most of the studied quasi-global domain, except over drier land and ocean regions such as Northern Africa, South Asia and Australia during dry seasons; and west coast of South America, Central America, and parts of North America, where locally the 95th percentile amount is very close to the mean precipitation value due to its small values and insignificant seasonal variations in precipitation. The 95th percentile precipitation varies greatly between months and seasons in some locations. For example, this seasonal variability is most apparent at sites in the north of Australia, where during the wet season (December-May) some locations experience 95th percentile rainfall higher than 50 mm day^{-1}, while during the drier months (June-November) the same locations show tiny rainfall values. A rough factor of 5-6 between the mean precipitation (R_{mean}) and R_{95p}, and a factor of 3-4 between the mean rain rate (R_{cond}) and R_{95p} is observed in the annual mean over the tropics that experiences most of the rainfall (figures not shown). Therefore, we investigate other similar statistical parameters that can better characterize the intense precipitation regime in recent years.

6.2. Mean and fraction of precipitation above the 95th percentile

While the R_{95p} parameter gives some insight into the distribution of heavy precipitation, other additional parameters need to be examined to offer more detailed explanations and relations of parameters that accent the intense precipitation. One such parameter that emphasizes the amount of precipitation occurring during intense events is

411   the monthly mean precipitation with rainfall $\geq 95^{th}$ percentile (R_{95}, in mm day^{-1}), defined

412   as the total amount of precipitation $\geq R_{95p}$ in a month divided by the number of days in

413   that month (see Table 1). The spatial patterns of R_{95} (Fig. 5) and R_{mean} (Fig. 1) are similar

414   over most regions, as expected, although the R_{95} patterns emphasize somewhat the areas

415   with heavy rainfall. However, the fraction of rainfall that exceeds the 95th percentile to

416   the mean rainfall ($F_{95}=R_{95}/R_{mean}$, figure not shown) tends to vary inversely to R_{95}. Over

417   areas of higher mean rain rates, the ratio F_{95} is 0.2 to 0.3, indicating that 20-30% of

418   monthly rain occurs at daily rates above or equal to the R_{95p} threshold. On the other hand,

419   in the areas with light rainfall, the ratio F_{95} is high (~0.8-1), because the R_{95p} threshold is

420   very close to the mean rain rate with only one or two rain events in the month that

421   account for all of the rain. Therefore, while both the R_{95} and F_{95} parameters are of

422   interest, they are of limited value in discerning spatial and temporal variations of heavy

423   rainfall.

424   *6.3. Mean and fraction of precipitation above fixed thresholds*

425   Floods and landslides are usually associated with an absolute amount of precipitation

426   physically related to overflowing banks and/or moving soil from a slope - not from

427   exceeding a local percentile threshold. So, another approach to investigate the intense

428   precipitation characteristics is to examine intense precipitation parameters by evaluating

429   the fraction of days in a month with precipitation that exceeds fixed threshold values

430   (e.g., 25, 50 and 75 mm day^{-1}; F_{25}, F_{50} and F_{75}). The maximum value observed in the

431   annual mean number of days with intense precipitation defined by the 95th percentile is

432   1.6 days/month (5%). Consequently, extremes based on the respective 95th percentile

433   (Fig. 4) show somewhat different spatial patterns than what is observed on maps of

434   fraction of days in a month with precipitation defined by any fixed thresholds over the

435   same locations and at the same time, due to a different selection of precipitation intensity

436   values.

437   The specific total daily precipitation threshold commonly used for determining

438   intense precipitation varies among regions and countries. A few examples of different

439   fixed thresholds, used by the national weather services or previous studies (e.g.,

440   Easterling et al. 2000; Gustafsson et al. 2010), give values of 20-40 mm day^{-1} for Norway

441   and Sweden, 20 mm day^{-1} for most of Russia and southern Canada, 50.8 mm day^{-1} for the

442   United States, Brazil, South Australia, northeastern China, Equatorial East Africa and

443   South Africa, and 100 mm day^{-1} for Japan and southeastern China.

444   In this study, characteristic spatial signatures of F_{25}, F_{50} and F_{75} for January and July

445   are compared to those observed in the mean precipitation (R_{mean}). The results show fairly

446   similar spatial patterns between these parameters, with a lower fraction of intense

447   precipitation by half going from 25 to 50 mm day^{-1}. The spatial distribution of monthly

448   mean frequency of intense rainfall (in days) suggest that local extremes in the tropics

449   occur mostly from June to August, with maximum values of 17, 10 and 6 days for the

450   three thresholds of 25, 50 and 75 mm day^{-1} (N_{25}, N_{50}, and N_{75}, figures not shown).

451   August noticeably receives the highest frequency of extremes for 25 and 50 mm day^{-1}

452   thresholds, while June receives it for 75 mm day^{-1} threshold. The period from September

453   to May is relatively quieter with respect to high season extremes, with maximum point

454   values of 14, 8 and 4 days observed for the three fixed thresholds. A strong seasonality of

455   intense precipitation frequency and its temporal dependence on the mean precipitation is

456   observed with clustering of extremes over the regions that experience the highest values

457   of mean precipitation.

458   Maps of climatological daily precipitation greater than several different thresholds

459   (i.e., above 0, 25 and 50 mm day^{-1}, and 95th percentile; R_{mean}, R_{25}, R_{50}, and R_{95}) show

460   their highest amounts over similar geographic areas both over land and ocean in the

461   annual and monthly climatologies. Fraction of days parameters with intense rainfall ≥ 25

462   and 50 mm day^{-1} (F_{25} and F_{50}) follow this similar spatial pattern that is observed in R_{mean}

463   as well.

464   Another measure of intense rainfall is the monthly mean rainfall ≥ 25 and 50 mm day^{-1}

465   (R_{25} and R_{50}, Fig. 6). The features here correspond well with spatial features previously

466   observed for the typical mean rainfall, but are weaker in intensity than for R_{mean} and

467   stronger than for R_{95}. Both R_{25} and R_{50} exhibit similar patterns, but a higher threshold

468   value of 50 mm day^{-1} filters out some of the extended features by depicting only areas

469   with higher amounts of rainfall. R_{25} can reach a maximum point value up to 24 mm day^{-1}

470   in January and 38 mm day^{-1} in July, with 20 mm day^{-1} in annual mean, but high values

471   have a range of 5-10 mm day^{-1} (Fig. 6a-c). Similarly, a maximum point value of R_{50} can

472   reach up to 20 mm day^{-1} in January and 34 mm day^{-1} in July, with 15 mm day^{-1} in annual

473   mean map (Fig. 6d-f), having high values between 3-8 mm day^{-1}. In comparison, R_{mean}

474   over the tropics has a maximum point value up to 27 mm day^{-1} in January and 43 mm

475   day^{-1} in July, with a maximum value of annual mean up to 24 mm day^{-1} (Fig. 1). From

476   monthly climatologies, April consistently exhibits the lowest amounts of R_{25} and R_{50},

477   similarly as observed in R_{mean}, R_{cond}, and R_{95}.

478   Based on the preceding analysis, R_{25} (Fig. 6a-c) is chosen to be a key parameter for

479   intense precipitation (hereafter intense precipitation). Therefore, we examine the intense

480   rainfall parameter in relation to the mean rainfall. The ratio F_{25}, defined as R_{25}/R_{mean},

481   gives the fraction of rain that falls above 25 mm in a day. Over a period of time (e.g., a

482   month), it is designed to emphasize areas and times when much of the rain falls during

483   days with intense rainfall. F_{25} (Fig. 7) shows some clear differences between two

484   parameters (R_{25} and R_{mean}), giving some characteristic spatial features that are not

485   observed in previously defined parameters, and some similar features that are wider in

486   coverage with a weaker gradient than what is observed for R_{cond} (a first measure of the

487   intensity examined in this study).

488   High intensity parameters are distributed both over land and ocean and higher in the

489   tropical latitudes. However, intense rainfall events with rain $\geq$25 mm day^{-1} are observed

490   somewhat more over ocean areas (Fig. 7) in comparison to the highest values of R_{cond} that

491   are located more over land (Fig. 3). On the annual map (Fig. 7a), maxima in F_{25} appear in

492   locations similar to those observed in R_{cond}, but also including more intensified locations

493   with wider spatial coverage over ocean and along the coasts, such as: east coast of

494   Australia, most of the mid-latitudes areas of both the Atlantic and Pacific Oceans, and

495   slightly wider equatorial Atlantic and Pacific Ocean regions (i.e., the ITCZ). A rough

496   factor of 0.65-0.75 for F_{25} is observed in the annual mean over the tropical region with

497   the highest rainfall amounts.

498   Strong seasonal variations in this intense rainfall measure are very similar to those

499   observed in R_{cond}. However, higher values of F_{25} (>0.6) are also observed mostly over the

500   extended tropical and mid-latitudes Southern Hemisphere ocean (7°N-35°S). Over land,

501 the highest values confirm intense events over Southeast Asian areas, related to the strong

502 monsoon phenomenon constantly switching between the Northern and Southern

503 Hemisphere. Similar features and high values over eastern China and the eastern U.S. are

504 associated with strong winter tropical cyclones in January (Fig. 7b). In addition, the most

505 significant features with high values in the Southern Hemisphere are located over a large

506 area of South America in January, while in July (austral winter, Fig. 7c) there are only

507 two maxima in intense rainfall, over the northern Amazonia and the La Plata basin. As

508 higher rainfall amounts tend to occur over previously mentioned moist regions, lower

509 rainfall tends to occur over the dryer regions with more intense convection (e.g., Sahel

510 and eastern Congo in Africa, and Argentina in South America).

511 Features in the monthly maps are consistently located over the areas where tropical

512 cyclones are most common (e.g., east of the Philippines, most of the Indian Ocean, and

513 the northern Gulf of Mexico) and over the La Plata basin, but also over the mountainous

514 regions with strong topographic lifting, where moderate and higher rainfall events last

515 longer. During Northern Hemisphere colder seasons (September-February), higher values

516 and wider spatial features of F_{25} are located over most of the northern Atlantic and

517 Pacific Oceans. During November-March, most observed maxima are located over the

518 wider SPCZ, and a persistently occurring feature across the La Plata basin and over

519 coastal waters in the southern Atlantic Ocean. Another set of maxima is located over the

520 persistent ITCZ and the east coast of Asia in the North Pacific Ocean during Northern

521 Hemisphere warm months (May-October). As observed, the ratio gives very strong

522 seasonal variations over most of the tropical regions. However, a quasi-global mean has a

523 typical value of only 0.34 during winter months (December, January and February) and

524 0.30 during summer months (July and August).

525   Statistical analysis of R_{25}, R_{50}, and R_{mean} during a 16-year climatological period

526 shows that intense rainfall is highly correlated with R_{mean}, with a correlation coefficient

527 (r) of 0.96 for R_{25} and 0.87 for R_{50} (significant at the 95% confidence level) on a monthly

528 time scale over the full domain examined. This highly correlated relationship between the

529 mean and intense precipitation parameters, and their spatial distribution, both over land

530 and ocean during the same time period, is confirmed in other data sets as well (e.g., over

531 the global domain in daily GPCP v1.2, and over the U.S. in daily National Oceanic and

532 Atmospheric Administration [NOAA] Climate Prediction Center [CPC] Unified Data,

533 results not shown here).

534   Fig. 8 shows distributions and correlations between mean precipitation and intense

535 precipitation (over ocean and land separately) using R_{25} and R_{50} as the parameters for the

536 intense component. Slightly lower correlations between intense and mean rainfall

537 parameters are observed when investigating land versus ocean amounts, for both fixed

538 threshold values (Fig. 8). The intense precipitation with the 50 mm day^{-1} fixed threshold

539 gives somewhat lower correlations (r=0.82 for land and 0.89 for ocean) and higher root-

540 mean-square (RMS) differences (3.08 mm day^{-1} for land and 3.00 mm day^{-1} for ocean)

541 than what is observed for the 25 mm day^{-1} threshold (r=0.95 for land and 0.97 for ocean)

542 with lower RMS differences (2.00 mm day^{-1} for land and 1.91 mm day^{-1}).

543   Figure 6 shows very characteristic spatial distributions over land and ocean, for both

544 R_{25} and R_{50}. The distribution of monthly climatology of R_{mean} against R_{25} (Fig. 8a-b), and

545 against R_{50} (Fig. 8c-d), is presented in such a way that all data values are divided into

546   bins in ascending order, including all grid points over the examined domain. Scatter plots

547   of intense precipitation against mean precipitation show a wider shape at the bottom of

548   the distribution and narrower but with a larger spread at the higher end of precipitation

549   values. There is no significant difference between land and ocean, except for a slightly

550   narrower distribution over ocean (Fig. 8a-b). We observe that the distribution becomes

551   slightly wider in shape with a lower slope of the median fit for a higher threshold chosen

552   (R_{50}, Fig. 8c-d).

553   A strong relationship between mean and intense precipitation is well defined by

554   fitting a median line over their spatial distribution. For the 25 mm day^{-1} threshold (Fig.

555   8a-b), a median fit is linear but with two different slopes: for smaller rainfall values

556   between 0-13 mm day^{-1} of R_{mean}, a slope for R_{25} is $R_{25}=0.65 \cdot R_{mean}$; and between 13-35

557   mm day^{-1} of R_{mean}, the slope increases to $R_{25}=1 \cdot R_{mean}$, both over land and ocean. In

558   comparison, the 50 mm day^{-1} threshold (Fig. 8c-d) gives results similar to the 25 mm day^{-}

559   ^{1} threshold for higher values (between 13-35 mm day^{-1} of R_{mean}, a slope for R_{50} equally

560   increases as in R_{25}, i.e., $R_{50}=1 \cdot R_{mean}$), but a decreased slope for the lower values (between

561   0-13 mm day^{-1} of R_{mean}, the slope for R_{50} decreases almost double with respect to R_{25},

562    $R_{50}=0.30 \cdot R_{mean}$). Above 20 mm day^{-1} of R_{mean}, there are a very few grid points per bin

563   observed (≤ 10 grids). However, up to that precipitation value we can well define the

564   median fit, which is consistent for the higher precipitation values as well. This result

565   offers a great method to estimate the intense precipitation (R_{25} or R_{50}) knowing a true

566   value of the mean precipitation (R_{mean}), and vice versa, on a local and global scale.

567   Overall, the observed high correlation values and a strong positive linear relationship

568   between intense precipitation and mean precipitation regimes, in terms of mean or total

569 accumulated amounts on a daily scale, build confidence in defining constant slopes

570 between them. This well-defined relationship and the ratio between two analyzed

571 parameters (R_{mean} and R_{25}) may therefore significantly help analyze current and past

572 intensity of rainfall amounts.

573   **7. Interannual variability of intense rainfall**

574   Numerous studies have shown that increase or reduction in mean precipitation are

575 likely to be associated with different phases of natural variability. For instance, recent

576 observations indicate that interannual climatic variability of mean precipitation is

577 strongly related to ENSO over many regions, and that a pronounced increase in intense

578 rainfall events is associated with warm or cold ENSO phases over many regions (e.g.,

579 IPCC 2007; Curtis et al. 2007; Grimm and Tedeschi 2009; Lau and Wu 2011).

580 Interdecadal modes of climate variability also produce changes in mean precipitation, as

581 well as in the frequency of extreme events (e.g., Grimm and Saboia 2015; Grimm et al.

582 2016). In order to focus on interannual variability of intense rainfall, we investigate both

583 El Niño and La Niña's influence on mean and intense precipitation.

584   There are just a few strong recent ENSO events observed during the 16-year period of

585 this study (e.g., El Niños in 1998, 2002-03, 2009-10, and La Niñas in 1998-99, 1999-

586 2000, 2007-08, 2010-11, 2011-12). The strength of ENSO is typically defined by using

587 the Niño3.4 monthly anomaly index of sea surface temperature. The Niño3.4 index over

588 the Niño3.4 region (5°N-5°S, 160°E-150°W) used here is obtained from NOAA CPC. El

589 Niño and La Niña periods are defined by choosing El Niño/La Niña months classified as

590 either the top third or bottom third of ranked monthly values of Niño3.4 index anomalies

591 during the available TMPA precipitation data record (1998-2013). Monthly Niño3.4

592   index values considered are then >0.14˚C and <-0.62˚C. Corresponding monthly values

593   of the TMPA 3B42 V7 precipitation anomalies of mean precipitation (e.g., R_{mean}) and

594   intense precipitation (e.g., R_{25} and R_{50}) are derived and analyzed for El Niño, La Niña

595   and neutral periods.

596   The strongest ENSO signal is observed over the Pacific and Indian Oceans; however,

597   ENSO also influences many other regions over the globe. Maps of seasonal mean

598   precipitation anomalies (R_{mean}) during El Niño period show: a strong precipitation

599   increase over the equatorial Pacific and Indian Oceans, the ITCZ and SPCZ tropical

600   regions, and a slight increase over the Southeast U.S. and the La Plata basin in South

601   America; and a decrease over the Maritime Continent, Amazonia, and the equatorial

602   Atlantic Ocean (Fig. 9a-d). During La Niña, a dipole regime observed in seasonal mean

603   precipitation anomalies is nearly opposite, as expected (Fig. 9e-h). The same persistent

604   regime is also observed in anomalies of mean and intense precipitation (R_{mean}, R_{25}, and

605   R_{50}) during both El Niño and La Niña periods (figures not shown). Figure 9 confirms the

606   strongest ENSO signal and the largest spatial coverage of rainfall amounts during

607   December-January-February (DJF) season, and the weakest signal with the smallest

608   spatial coverage during June-July-August (JJA) season, both for El Niño and La Niña

609   periods, respectively.

610   In a similar way to the monthly analysis of intense rainfall, we investigate a

611   relationship between anomalies of mean precipitation (R_{mean}) and intense precipitation

612   (e.g., R_{25}) for El Niño, La Niña, and neutral months. Figure 10 shows a set of scatter plots

613   between R_{mean} and R_{25} anomalies during El Niño, La Niña, and neutral periods, over

614   tropical land and ocean. The most pronounced variations in mean precipitation anomalies

615   and the highest maximums in intense precipitation anomalies are observed in the tropics.

616   Therefore, we investigate this strong positive relationship between two parameters for the

617   narrower tropical region (23.5°N-23.5°S). Mean and intense precipitation anomalies in

618   the scatter plots show slightly different characteristics during El Niño versus La Niña

619   periods, with a shift towards more positive versus negative anomalies (red/yellow colors

620   in Fig. 10). With a higher number of grid points (such as over ocean), a tail of the

621   observed linear distribution is longer, both in positive and negative anomalies. Similarly,

622   as expected, a shorter extension of the distribution is observed over land, confirming the

623   highest intense rainfall amounts mostly over the tropical oceans.

624   The results also give consistently higher amounts of positive heavy rainfall anomalies

625   during La Niña period over tropical land and especially during El Niño period over

626   tropical ocean (up to 4 mm day^{-1}), observed as an extension of the slightly wider

627   distribution with a larger number of grid points (Fig. 10b,d). In contrast, higher amounts

628   of negative heavy rainfall anomalies are observed during El Niño over land (up to -3.5

629   mm day^{-1}) and during La Niña over ocean (up to -4.3 mm day^{-1}; Fig. 10a,e). This is all

630   due to placement of land (e.g., South America) in relation to the precipitation variations.

631   The distribution of intense and mean precipitation anomalies for neutral period gives

632   significantly lower rainfall amounts (in a range of ±2 mm day^{-1}), with more uniform and

633   symmetrical shape, both over land and ocean. Higher correlations between R_{mean} and R_{25}

634   anomalies are observed during El Niño and La Niña periods (r=0.92 for land and r=0.97-

635   0.98 for ocean) versus neutral periods (0.88 for land and 0.94 for ocean). Slightly higher

636   correlations observed over ocean in individual El Niño/La Niña period are probably due

637   to more uniform rainfall data over ocean than over land. A slope of the positive linear

median fit in the distributions of R_{mean}-R_{25} anomalies is very similar and consistent for El Niño and La Niña periods, and slightly higher over land than over ocean (R_{25}=0.75·R_{mean} for land and R_{25}=0.65·R_{mean} for ocean, Fig. 10a-b,d-e). As noted above, neutral periods experience much lower change in mean and intense rainfall amounts, but a higher slope of the linear median fit (R_{25}=0.90·R_{mean} for land and R_{25}=0.85·R_{mean} for ocean, Fig. 10c,f).

Results similar to those for R_{25} are observed for the R_{50} distribution over the tropics as well (figure not shown). However, with the higher daily threshold of 50 mm day^{-1}, overall change in R_{50} is even lower than the observed change in R_{mean}, with a decreased slope of the linear median fit in the distribution of rainfall anomalies (a change factor of 0.40-0.50 during El Niño/La Niña period and 0.65-0.70 during neutral period). The R_{mean}-R_{50} distribution gives a wider shape of observed anomalies and slightly lowers correlations both over land and ocean (0.88-0.98 for R_{25} vs. 0.70-0.88 for R_{50}).

8. Regions with intense rainfall strongly related to ENSO

A few interesting regions located in areas with the observed peaks in mean and intense precipitation are chosen for a more detailed analysis of interannual variability of intense rainfall. The first region is defined over the West Pacific Ocean, as a 5°x5° grid box (6°S-1°S, 177°E-182°E), over which an average of R_{mean}, R_{25} and R_{50} is computed (Fig. 11). Corresponding time series are analyzed then over the highest amounts of rainfall, showing the overall variability of intense precipitation (R_{25} and R_{50}), following closely the mean rainfall variation of R_{mean}. As expected, high correlations between mean and intense precipitation anomalies (r=0.99 for R_{25} and 0.95 for R_{50}) are observed over the West Pacific Ocean region (Fig. 11a).

661   The same parameters are also analyzed in relation to the Niño3.4 index. A scatter plot

662   of mean and intense precipitation anomalies with respect to the Niño3.4 index anomalies

663   shows a strong positive linear relationship (Fig. 11b). High correlations of 0.66 for R_{25}

664   and 0.61 for R_{50} (both significant at the 95% confidence level) between the Niño3.4 index

665   and intense precipitation anomalies are observed over the West Pacific Ocean region.

666   R_{mean} gives slightly higher correlation of 0.70 with the Nino3.4 index.

667   The West Pacific region is then compared with a 5°x5° region over the Philippines

668   (10°N-15°N, 122°E-127°E) that includes both land and ocean areas, to address main

669   differences between these two regions experiencing the opposite extreme sign in R_{mean},

670   R_{25} and R_{50} anomalies (Fig. 12). The scatter plots of mean and intense precipitation

671   anomalies show strong positive values during El Niño period (red color values in Fig.

672   12a) and strong negative values during La Niña period (blue color values in Fig. 12a)

673   over the West Pacific Ocean region, and the opposite dipole regime with strong positive

674   values during La Niña and strong negative values during El Niño period over the

675   Philippines region (Fig. 12b). During neutral period, anomalies are distributed around a

676   center of the scatter plots. Two contrasting regions give high correlations between mean

677   and intense precipitation anomalies (0.99 for R_{25} and 0.95 for R_{50} over the Pacific region,

678   and 0.98 for R_{25} and 0.94 for R_{50} over the Philippines) and significantly small RMS

679   differences (1.15 mm day^{-1} for R_{25} and 2.23 mm day^{-1} for R_{50} over the Pacific region, and

680   0.72 mm day^{-1} for R_{25} and 1.43 mm day^{-1} for R_{50} over the Philippines).

681   Another pair of smaller secondary peaks in R_{mean}, R_{25} and R_{50} anomalies is observed

682   over the continental South America in the La Plata basin (33°S-28°S, 299°E-304°E) and

683   in central Amazonia (5°S-0°, 301°E-306°E). Both regions over the South American land

684 experience strong ENSO signal, but with somewhat weaker precipitation anomalies and a

685 lower R_{25}/R_{mean} ratio than observed in the Pacific/Philippines regions during El Niño/La

686 Niña period. All regions show consistently high significant correlations ranging between

687 0.95-0.99 for R_{25} and 0.81-0.96 for R_{50}, with a strong positive linear fit. However, the

688 Pacific/Philippines distributions show higher RMS differences of 0.72-1.15 mm day^{-1} for

689 R_{25} and 1.43-2.23 mm day^{-1} for R_{50} versus South American 0.36-0.71 mm day^{-1} for R_{25}

690 and 0.84-1.33 mm day^{-1} for R_{50} (Fig. 12), and this is due to higher rainfall variability over

691 ocean. In addition, El Niño/La Niña identified values over the South American land are

692 not separated in the way they are over the West Pacific/Philippines regions and somewhat

693 in the La Plata basin (distributed only as positive or negative anomalies during El Niño or

694 La Niña, seen in Fig. 12c-d vs. 12a-b), indicating that other factors, besides ENSO, must

695 play a role there. In the La Plata basin, besides mid-latitude effects, there are also other

696 influences from the Pacific and Atlantic Oceans, which play an even more significant role

697 in the Amazon region. They can be similar or opposite to the ENSO influence, enhancing

698 or weakening the resulting effect on both inter-annual and inter-decadal time scales

699 (Grimm 2011; Grimm and Saboia 2015).

700 **9. Discussion and conclusions**

701 Satellite-based estimation of precipitation, specifically the TRMM-based TMPA

702 3B42 V7 analysis has allowed us to examine climatology and variations of recent intense

703 daily precipitation during 1998-2013. This study analyzes different parameters

704 representing mean and intense precipitation, their relationships and variability,

705 contributing to our understanding of the precipitation behavior at climate scale. The

706 relatively short 16-year data record used here limits our examination of extreme daily

707 precipitation, but allows for a careful study of intense daily precipitation, including its

708 climatology and variations that should be related to events such as floods and landslides.

709 This capability is due to the TMPA's relatively high quality, i.e., mostly microwave-

710 based, high resolution (3-hr, 0.25° lat./lon.), continual calibration, continuity, and

711 uniformity over a near-global domain (50°N-50°S).

712 Climatologies of mean rainfall, conditional mean rainfall and fraction of rainfall days

713 are examined and compared, and begin to reveal areas and times where and when heavier

714 rainfall is more frequent. We tested several commonly used parameters to define intense

715 precipitation, such as: mean monthly 95th percentile of daily precipitation, mean and

716 fraction of precipitation that exceeds the 95th percentile, fraction of intense precipitation

717 above fixed daily thresholds of 25 and 50 mm day^{-1}, and mean rainfall above same fixed

718 thresholds, to infer which parameter best characterizes the heavy rainfall regime. Spatial

719 patterns and features of various mean and intense precipitation parameters compare well

720 to each other, with some differences over land and ocean. The overall results show a very

721 strong relationship between mean and intense precipitation. Specifically, consistently

722 high significant correlations with a strong positive linear relationship are observed

723 between two interesting parameters: the monthly mean precipitation (mean precipitation

724 ≥ 0 mm day^{-1}, R_{mean}) and intense precipitation (mean precipitation ≥ 25 mm day^{-1}, R_{25}).

725 Among the various examined parameters, the one best characterizing the intense

726 rainfall is observed to be a ratio between intense precipitation and mean precipitation

727 (R_{25}/R_{mean}). This ratio is considered to be a good measure of rainfall intensity. The results

728 show high significant correlations and a strong positive linear relationship between these

729 two parameters (R_{25} and R_{mean}), explaining the contribution of intense rainfall to total

730   rainfall. We consider this analysis to be a first attempt of this kind to determine the best

731   measure for intense rainfall.

732   From analysis of interannual variability of intense precipitation, we confirm a strong

733   positive linear relationship and consistently high correlations between mean and intense

734   precipitation anomalies, especially during El Niño and La Niña periods. The results also

735   confirm that El Niño and La Niña events with their effects equally contribute to the

736   observed connection between mean and intense precipitation, with no significant

737   difference between land and ocean. In general, most of the intense rainfall events are

738   observed over tropical ocean. However, the results show that intense rainfall events are

739   stronger and more frequent during La Niña periods over tropical land and during El Niño

740   periods over tropical ocean. Overall, the observed change in intense rainfall anomalies is

741   lower than the one observed in mean rainfall anomalies during El Niño/La Niña period,

742   and it decreases with a higher fixed threshold (a factor of 0.65-0.75 for R_{25} and 0.40-0.50

743   for R_{50}).

744   Intense rainfall is the major factor of causing floods and landslides worldwide,

745   especially in recent years. Therefore, improved knowledge of the intense precipitation

746   regime and its strong connection to the mean precipitation on a global to regional scale

747   can offer more consistent current and near-future estimates of heavy rainfall, providing

748   help in preventing damages caused by extreme events (i.e., floods, flash floods, and

749   landslides). Future research should focus on the analysis of intense precipitation and

750   flood events, together with economic and social systems, including additional factors

751   such as population, critical infrastructures, and financial indices of cost that help estimate

752   the potential risks and impacts of extreme and heavy rainfall events. Providing accurate

753 estimates of future intense precipitation events due to climate change, global warming,

754 and/or natural climate variability (i.e., ENSO) is crucial.

755   For the future, the Global Precipitation Measurement (GPM) mission will

756 significantly contribute to an improved record of intense precipitation, extending to a

757 more global domain, and allowing for a longer, enhanced climate record to be used. This

758 should allow a better specification of the intense precipitation relationships in the coming

759 years.

References

1. Adler, R. F., and Coauthors, 2003: The Version-2 Global Precipitation Climatology Project (GPCP) monthly precipitation analysis (1979–present). *J. Hydrometeor.*, **4**, 1147–1167, doi:10.1175/1525-7541(2003)004<1147:TVGPCP>2.0.CO;2.

2. Adler, R. F., G. Gu, J.-J. Wang, G. J. Huffman, S. Curtis, and D. Bolvin, 2008: Relationships between global precipitation and surface temperature on interannual and longer timescales (1979–2006). *J. Geophys. Res.*, **113**, D22104, doi:10.1029/2008JD010536.

3. Adler, R. F., J.-J. Wang, G. Gu, and G. J. Huffman, 2009: A ten-year tropical rainfall climatology based on a composite of TRMM products. *J. Meteor. Soc. Japan*, **87A**, 281–293, doi:10.2151/jmsj.87A.281.

4. Allan, R. P., and B. J. Soden, 2008: Atmospheric Warming and the Amplification of Precipitation Extremes. *Science,* **321,** 1481-1484, doi:10.1126/science.1160787.

5. Arkin, P. A., J. Turk, and E. Ebert, 2008: Pilot Evaluation of High Resolution Precipitation Products (PEHRPP): A contribution to GPM planning.

6. Benestad, R. E., D. Nychka, and L. O. Mearns, 2012: Spatially and temporally consistent prediction of heavy precipitation from mean values. *Nat. Clim. Change*, **2**, 544-547, doi:10.1038/NCLIMATE1497.

7. *Benestad, R. E., 2013: Association between trends in daily rainfall percentiles and the global mean temperature. *J. Geophys. Res. Atmos.,* **118**, 10802–10810, doi:10.1002/jgrd.50814.*

790   8. Cavalcanti, I. F. A., 2012: Large scale and synoptic features associated with

791   extreme precipitation over South America: A review and case studies for the first

792   decade of the 21st century. *Atmos. Res.*, **118**, 27-40,

793   doi:10.1016/j.atmosres.2012.06.012.

794   9. Curtis, S., A. Salahuddin, R. F. Adler, G. J. Huffman, G. Gu, and Y. Hong, 2007:

795   Precipitation Extremes Estimated by GPCP and TRMM: ENSO Relationships. *J.*

796   *Hydrometeor.*, **8**, 678–689, doi:10.1175/JHM601.1.

797   10. Dai, A., I. Y. Fung, and A. D. Del Genio, 1997: Surface observed global land

798   precipitation variations during 1900–88. *J. Climate*, **10**, 2943–2962,

799   doi:10.1175/1520-0442(1997)010<2943:SOGLPV>2.0.CO;2.

800   11. Dai, A., 2011: Drought under global warming: A review. *Wiley Interdisciplinary*

801   *Reviews: Climate Change*, **2**, 45-65, doi:10.1002/wcc.81.

802   12. Easterling, D. R., J. L. Evans, P. Y. Groisman, T. R. Karl, K. E. Kunkel, and P.

803   Ambenje, 2000: Observed variability and trends in extreme climate events: A

804   brief review. *Bull. Amer. Meteor. Soc.*, **81**, 417–425, doi:10.1175/1520-

805   0477(2000)081<0417:OVATIE>2.3.CO;2.

806   13. Ebert, E. E., J. Janowiak, and C. Kidd, 2007: Comparison of near-real time

807   precipitation estimates from satellite observations and numerical models. *Bull.*

808   *Amer. Meteor. Soc.*, **88**, 47–64, doi:10.1175/BAMS-88-1-47.

809   14. Grimm, A. M., and R. G. Tedeschi, 2009: ENSO and extreme rainfall events in

810   South America. *J. Climate*, **22**, 1589-1609, doi:10.1175/2008JCLI2429.1.

811   15. Grimm, A. M., 2011: Interannual climate variability in South America: impacts

812   on seasonal precipitation, extreme events, and possible effects of climate change.

813   *Stoch. Environ. Res. Risk. Assess.*, **25**, 537-554, doi:10.1007/s00477-010-0420-1.

814   16. Grimm, A. M. and J. P. J. Saboia, 2015: Interdecadal Variability of the South

815   American Precipitation in the Monsoon Season. *J. Climate*, **28**, 755-775,

816   doi:10.1175/JCLI-D-14-00046.1.

817   17. Grimm, A. M., N. C. Laureanti, R. B. Rodakoviski, and C. B. Gama, 2016:

818   Interdecadal variability and extreme precipitation events in South America during

819   the monsoon season. *Climate Research*, **68**, 2-3, doi: 10.3354/cr01375.

820   18. Gu, G., R. F. Adler, G. J. Huffman, and S. Curtis, 2007: Tropical Rainfall

821   Variability on Interannual-to-Interdecadal and Longer Time Scales Derived from

822   the GPCP Monthly Product. *J. Climate*, **20**, 4033–4046, doi:10.1175/JCLI4227.1

823   19. Gustaffson, M., D. Rayner, and D. Chen, 2010: Extreme rainfall events in

824   southern Sweden: where does the moisture come from? *Tellus*, **62A**, 605-616,

825   doi:10.1111/j.1600-0870.2010.00456.x.

826   20. Held, I. M., and B. J. Soden, 2006: Robust responses of the hydrological cycle to

827   global warming. *J. Clim*ate, **19**, 5686–5699, doi:10.1175/JCLI3990.1.

828   21. Huffman, G. J., R. F. Adler, M. Morrissey, D. Bolvin, S. Curtis, R. Joyce, B.

829   McGavock, and J. Susskind, 2001: Global precipitation at one-degree daily

830   resolution from multi-satellite observations. *J. Hydrometeor*., **2**, 36-50,

831   doi:10.1175/1525-7541(2001)002<0036:GPAODD>2.0.CO;2.

832   22. Huffman, G. J., and Coauthors, 2007: The TRMM Multisatellite Precipitation

833   Analysis (TMPA): Quasi-Global, Multiyear, Combined-Sensor Precipitation

834   Estimates at Fine Scales. *J. Hydrometeor.*, **8**, 38–55, doi:10.1175/JHM560.1.

835   23. Huffman, G. J., R. F. Adler, D. T. Bolvin, and G. Gu, 2009: Improving the global

836   precipitation record: GPCP Version 2.1. *Geophys. Res. Lett.*, **36**, L17808,

837   doi:10.1029/2009GL040000.

838   24. Huffman, G. J., R. F. Adler, D. T. Bolvin, and E. J. Nelkin, 2010: The TRMM

839   Multi-satellite Precipitation Analysis (TMPA). Chapter 1 in *Satellite Rainfall*

840   *Applications for Surface Hydrology*, F. Hossain and M. Gebremichael, Eds.,

841   Springer Verlag, ISBN: 978-90-481-2914-0, 3-22. [Available online at

842   ftp://precip.gsfc.nasa.gov/betsy/huffman/papers/TMPA_hydro_rev.pdf.]

843   25. Huffman, G. J., and D. T. Bolvin, 2012: TRMM and Other Data Precipitation

844   Data Set Documentation. Technical product document, 1-37. [Available online at

845   ftp://trmmopen.gsfc.nasa.gov/pub/merged/V7Documents/3B4XRT_doc_V7.pdf.]

846   26. IPCC, 2007. *Climate Change 2007: The Physical Science Basis*, S. Solomon, D.

847   Qin, M. Manning, Z. Chen, M. Marquis, K. B. Averyt, M. Tignor, H. L. Miller,

848   Eds., Contribution of Working Group I to the Fourth Assessment Report of the

849   Intergovernmental Panel on Climate Change, Cambridge University Press,

850   Cambridge, United Kingdom/New York, NY, USA, 996 pp.

851   27. Karl, T. R., N. Nicholls, and A. Ghazi, 1999: CLIVAR/GCOS/WMO workshop

852   on indices and indicators for climate extremes: Workshop summary. *Climatic*

853   *Change*, **42**, 3-7, doi:10.1023/A:1005491526870.

854   28. Kharin, V., F. W. Zwiers, X. Zhang, and G. C. Hergerl, 2007: Changes in

855   temperature and precipitation extremes in IPCC ensemble of coupled model

856   simulations. *J. Climate*, **20**, 1419–1444, doi:10.1175/JCLI4066.1.

857   29. Kirschbaum, D., R. Adler, D. Adler, C. Peters-Lidard, and G. Huffman, 2012:

858   Global Distribution of Extreme Precipitation and High-Impact Landslides in 2010

859   Relative to Previous Years. *J. Hydrometeor.*, **13**, 1536–1551, doi:10.1175/JHM-

860   D-12-02.1.

861   30. Lau, K.-M., and H.-T. Wu, 2011: Climatology and changes in tropical oceanic

862   rainfall characteristics inferred from Tropical Rainfall Measuring Mission

863   (TRMM) data (1998-2009). *J. Geophys. Res.*, **116**, D17111,

864   doi:10.1029/2011JD015827.

865   31. Lau, W. K.-M., H.-T. Wu, and K.-M. Kim, 2013: A canonical response of

866   precipitation characteristics to global warming from CMIP5 models. *Geophys.*

867   *Res. Lett.*, **40**, 3163–3169, doi:10.1002/grl.50420.

868   32. Liu, C. and R. P. Allan, 2012: Multi-satellite observed responses of precipitation

869   and its extremes to interannual climate variability. *J. Geophys. Res.,* **117,** D03101,

870   doi:10.1029/2011JD016568.

871   33. Min, S-K., X. Zhang, F. W. Zwiers, and G. C. Hegerl, 2011: Human contribution

872   to more-intense precipitation extremes. *Nature*, **470**, 378-381,

873   doi:10.1038/nature09763.

874   34. O'Gorman, P.A., 2012: Sensitivity of tropical precipitation extremes to climate

875   change. *Nature Geoscience*, **5**, 697-700, doi:10.1038/ngeo1568.

876   35. Peterson, T.C., C. Folland, G. Gruza, W. Hogg, A. Mokssit, and N. Plummer,

877   2001: Report on the Activities of the Working Group on Climate Change

878   Detection and Related Rapporteurs 1998-2001. *World Meteorological*

879   *Organization*, Rep. WCDMP-47, WMO-TD 1071, Geneva, Switzerland, 143 pp.

880   36. Sapiano, M. R. P., and P. A. Arkin, 2009: An inter-comparison and validation of

881   high resolution satellite precipitation estimates with three-hourly gauge data. *J.*

882 *Hydrometeor.,* **10**(1), 149-166, doi:10.1175/2008JHM1052.1.

883 37. Scheel, M. L. M., M. Rohrer, C. Huggel, D. S. Villar, E. Silvestre, and G. J.

884   Huffman, 2011: Evaluation of TRMM Multi-satellite Precipitation Analysis

885   (TMPA) performance in the Central Andes region and its dependency on spatial

886   and temporal resolution. *Hydrol. Earth Syst. Sci.*, **15**, 2649-2663,

887   doi:10.5194/hess-15-2649-2011.

888 38. Schneider, U., A. Becker, A. Meyer-Christoffer, M. Ziese and B. Rudolf, 2011:

889   Global Precipitation Analysis Products of the GPCC. Global Precipitation

890   Climatology Centre (GPCC), DWD, Internet Publikation, 13 pp.

891 39. Shiu, C.-J., S. C. Liu, C. Fu, A. Dai, and Y. Sun, 2012: How much do

892   precipitation extremes change in a warming climate? *Geophys. Res. Lett*., **39**,

893   L17707, doi:10.1029/2012GL052762.

894 40. Su, F., Y. Hong, and D. P. Lettenmaier, 2008: Evaluation of TRMM Multisatellite

895   Precipitation Analysis (TMPA) and its utility in hydrologic prediction in the La

896   Plata basin. *J. Hydrometeor*., **9**, 622–640, doi:10.1175/2007JHM944.1.

897 41. Tian, Y., and Coauthors, 2009: Component analysis of errors in satellite-based

898   precipitation estimates. *J. Geophys. Res*., **114**, D24101,

899   doi:10.1029/2009JD011949.

900 42. Trenberth, K. E., A. Dai, R. M. Rasmussen, and D. B. Parsons, 2003: The

901   changing character of precipitation. *Bull. Amer. Meteor. Soc*., **84**, 1205–1217,

902   doi:10.1175/BAMS-84-9-1205.

903   43. Wang, J.-J., R. F. Adler, G. J. Huffman, and D. Bolvin, 2014: An updated TRMM

904   composite climatology of tropical rainfall and its validation. *J. Climate*, **27**, 273-

905   284, doi:10.1175/JCLI-D-13-00331.1.

906   44. Wu H., R. F. Adler, Y. Hong, Y. Tian, and F. Policelli, 2012: Evaluation of

907   Global Flood Detection Using Satellite-Based Rainfall and a Hydrologic Model.

908   *J. Hydrometeor.*, **13**, 1268–1284, doi:10.1175/JHM-D-11-087.1.

909 **Figure Captions**

910 **Figure 1** (a) Annual, (b) January, and (c) July mean precipitation climatology (R_{mean}, mm

911 day^{-1}), derived from the TMPA 3B42 Version 7 data during 1998-2013.

912 **Figure 2** (a) Annual, (b) January, and (c) July mean climatological fraction of days with

913 precipitation >0 mm day^{-1} ($F_0=R_{mean}/R_{cond}$), derived from the TMPA 3B42 Version 7 data

914 during 1998-2013.

915 **Figure 3** (a) Annual, (b) January, and (c) July mean climatological conditional

916 precipitation rate (R_{cond}, mm day^{-1}), derived from the TMPA 3B42 Version 7 data during

917 1998-2013.

918 **Figure 4** (a) Annual, (b) January, and (c) July mean 95th percentile daily precipitation

919 value (R_{95p}, mm day^{-1}), derived from the TMPA 3B42 Version 7 data during 1998-2013.

920 **Figure 5** (a) Annual, (b) January, and (c) July mean precipitation $\geq 95^{th}$ percentile daily

921 precipitation (R_{95}, mm day^{-1}), derived from the TMPA 3B42 Version 7 data during 1998-

922 2013.

923 **Figure 6** Annual, January, and July mean precipitation (a)-(c) ≥ 25 mm day^{-1} threshold

924 (R_{25}; mm day^{-1}) and (d)-(f) ≥ 50 mm day^{-1} threshold (R_{50}; mm day^{-1}), derived from the

925 TMPA 3B42 Version 7 data during 1998-2013.

926 **Figure 7** (a) Annual, (b) January, and (c) July mean climatological fraction of daily

927 precipitation ≥ 25 mm day^{-1} ($F_{25}=R_{25}/R_{mean}$), derived from the TMPA 3B42 Version 7

928 data during 1998-2013.

929 **Figure 8** Scatter plots of monthly climatology of mean precipitation (R_{mean}, mm day^{-1})

930 and intense precipitation (a)-(b) ≥ 25 mm day^{-1} (R_{25}, mm day^{-1}) and (c)-(d) ≥ 50 mm day^{-1}

931 (R_{50}, mm day^{-1}) over the TRMM domain (50°N-50°S), separately over land and ocean,

932 derived from the TMPA 3B42 Version 7 data during 1998-2013. The color bar indicates

933 the number of grid points with the attributed values in a logarithmic scale. Median (black

934 dashed line) is calculated for a distribution of all 12 months. Correlation coefficient and

935 RMS difference between intense rainfall (R_{25} and R_{50}) and R_{mean} are displayed.

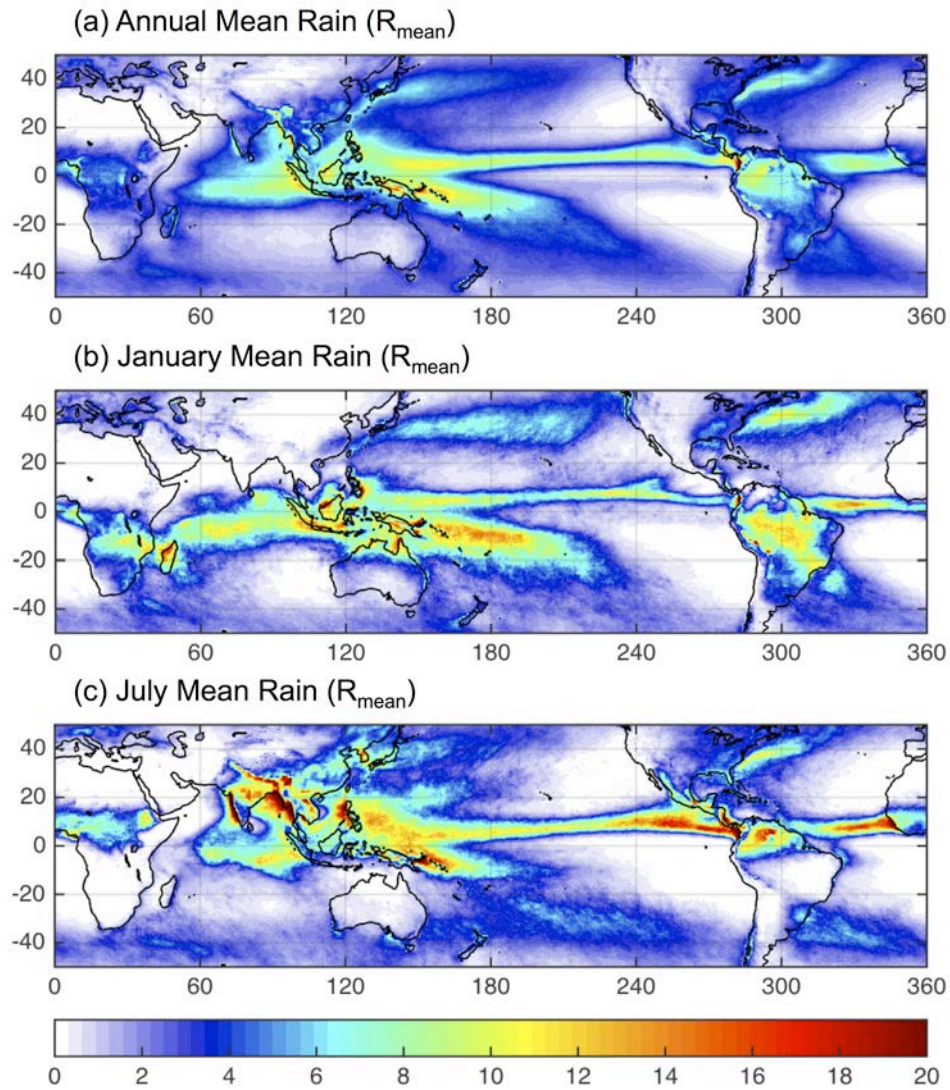936 Correlation values are significant at the 95% confidence level.

937 **Figure 9** Mean precipitation anomalies (mm day^{-1}) for 4 seasons (DJF, MAM, JJA, SON)

938 for (a)-(d) El Niño and (e)-(h) La Niña period, derived from the TMPA 3B42 Version 7

939 data during 1998-2013.

940 **Figure 10** Scatter plots of mean precipitation (R_{mean}, mm day^{-1}) and intense precipitation

941 $\geq$25 mm day^{-1} (R_{25}, mm day^{-1}) anomalies for El Niño, La Niña and neutral period, over

942 the tropical domain (23.5°N-23.5°S), over (a)-(c) land and (d)-(f) ocean, derived from the

943 TMPA 3B42 Version 7 data during 1998-2013. The color bar indicates the number of

944 grid points with the attributed values in a logarithmic scale. Correlation coefficient

945 between R_{25} and R_{mean} is displayed. Correlation values are significant at the 95%

946 confidence level.

947 **Figure 11** (a) Time series of mean precipitation (R_{mean}, mm day^{-1}; blue line) and intense

948 precipitation $\geq$25 mm day^{-1} (R_{25}, mm day^{-1}; black line) and $\geq$50 mm day^{-1} (R_{50}, mm day^{-1};

949 red line) anomalies, and (b) scatter plot of R_{mean}, R_{25}, and R_{50}, and Niño3.4 index

950 anomalies, averaged over a 5°x5° box over the West Pacific Ocean (6°S-1°S, 177°E-

951 182°E), derived from the TMPA 3B42 Version 7 precipitation data during 1998-2013.

952 Correlation coefficient and RMS difference between intense rainfall (R_{25} and R_{50}) and

953 R_{mean} are displayed in (a), and correlation coefficient between R_{mean}, R_{25}, and R_{50} with

954   respect to the Niño3.4 index in (b). Correlation values are significant at the 95%

955   confidence level.

956   **Figure 12** Scatter plots of mean precipitation (R_{mean}; mm day^{-1}) and intense precipitation

957     $\geq$25 mm day^{-1} (R_{25}, mm day^{-1}; filled circles and black line) and $\geq$50 mm day^{-1} (R_{50}, mm

958   day^{-1}; empty circles and red line) anomalies, with corresponding linear fit for El Niño

959   (red), La Niña (blue) and neutral period (black), averaged over a 5°x5° box over: (a) the

960   West Pacific Ocean, (b) Philippines, (c) La Plata basin, and (d) Amazonia, derived from

961   the TMPA 3B42 Version 7 data during 1998-2013. 5°x5° boxes are chosen denoting two

962   largest maximums and minimums observed in global anomalies. Correlation coefficient

963   and RMS difference between intense rainfall (R_{25} and R_{50}) and R_{mean} are displayed.

964   Correlation values are significant at the 95% confidence level.

965 **Table Captions**

966 **Table 1** Definitions and units for monthly parameters of mean and intense precipitation**.**

967 **Tables**

968 **Table 1** Definitions and units for monthly parameters of mean and intense precipitation.

Definition	Parameter	Unit
Daily precipitation	R	mm day^{-1}
MEAN PRECIPITATION:		
Monthly mean precipitation (total amount of precipitation in a month/total days in a month)	R_{mean}	mm day^{-1}
Mean conditional precipitation rate (mean precipitation rate for days with R >0 mm day^{-1})	R_{cond}	mm day^{-1}
Fraction of days in a month with R >0 mm day^{-1} (R_{mean}/R_{cond})	F_0	
INTENSE PRECIPITATION:		
95th percentile of daily precipitation in a month	R_{95p}	mm day^{-1}
Monthly mean precipitation with R $\geq$95th percentile (Total R $\geq R_{95p}$ in a month/total days in a month)	R_{95}	mm day^{-1}
Fraction of daily precipitation with R $\geq$95th percentile (R_{95}/R_{mean})	F_{95}	
Monthly mean precipitation with R $\geq$25 and 50 mm day^{-1} (Total R $\geq$25 and 50 mm day^{-1} in a month/total days in a month)	R_{25}, R_{50}	mm day^{-1}
Number of days within a month with R $\geq$25, 50 and 75 mm day^{-1} threshold	N_{25}, N_{50}, N_{75}	day
Fraction of daily precipitation with R $\geq$25 and 50 mm day^{-1} (R_{25}/R_{mean} and R_{50}/R_{mean})	F_{25}, F_{50}	

Figures

(a) Annual Mean Rain (R_{mean})

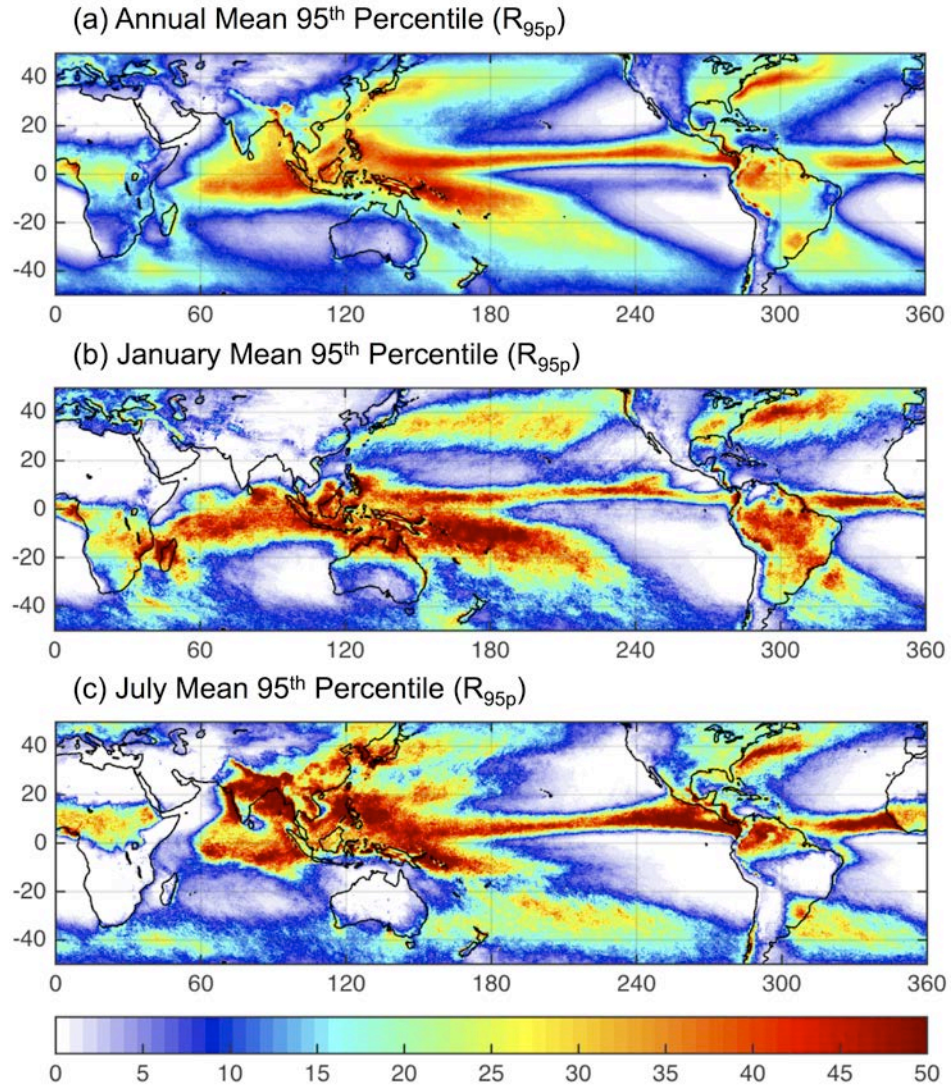## (b) January Mean Rain (R_{mean})

(c) July Mean Rain (R_{mean})

970
971 **FIG. 1.** (a) Annual, (b) January, and (c) July mean precipitation climatology (R_{mean}, mm
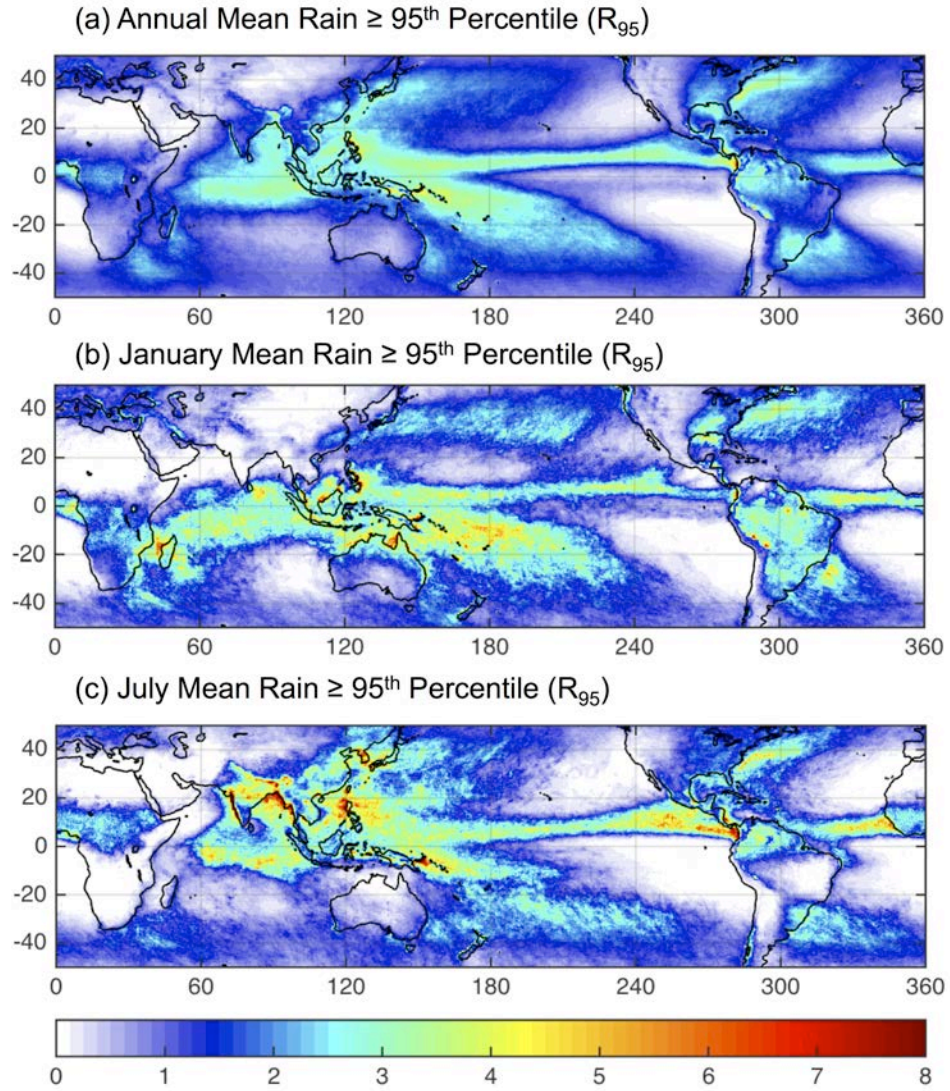972 day^{-1}), derived from the TMPA 3B42 Version 7 data during 1998-2013.

(a) Annual Mean Fraction of Days with Rain > 0 (F_0)

(b) January Mean Fraction of Days with Rain > 0 (F_0)

(c) July Mean Fraction of Days with Rain > 0 (F_0)
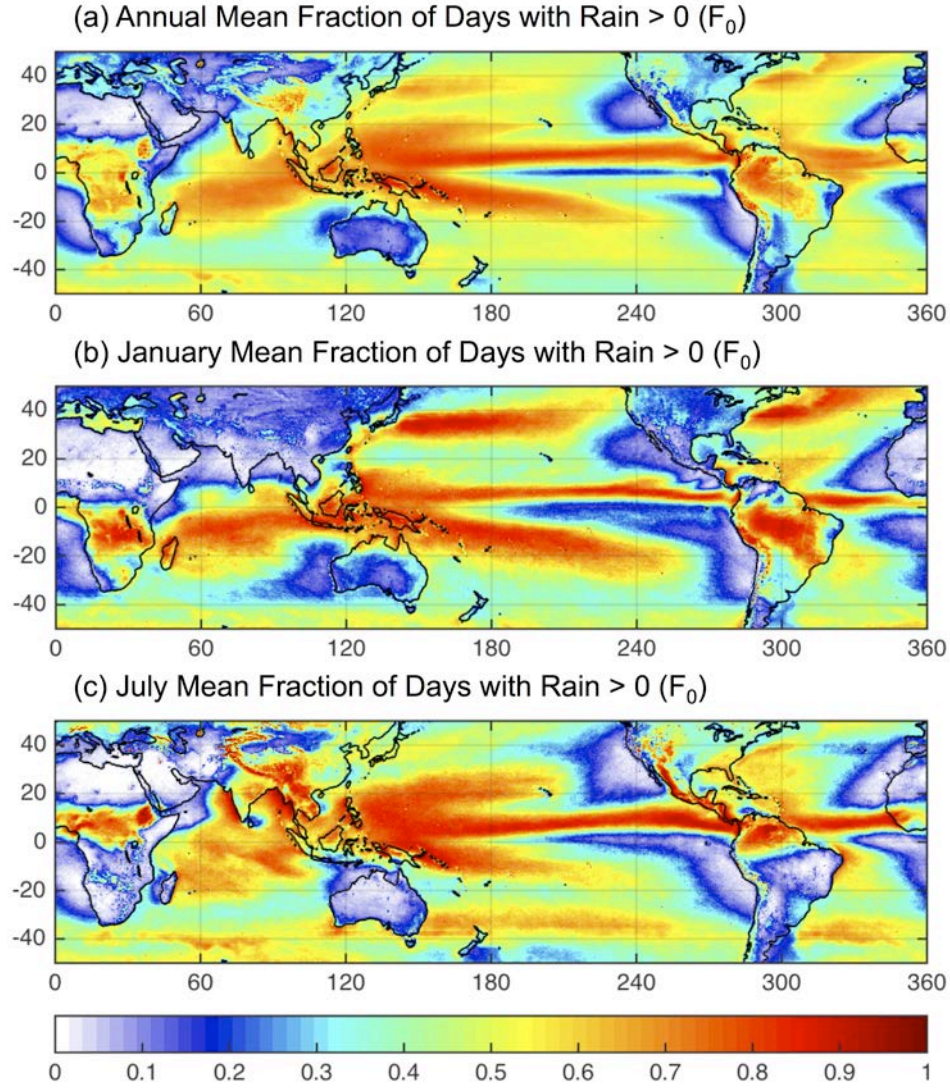
FIG. 2. (a) Annual, (b) January, and (c) July mean climatological fraction of days with precipitation >0 mm day^{-1} ($F_0 = R_{mean}/R_{cond}$), derived from the TMPA 3B42 Version 7 data during 1998-2013.
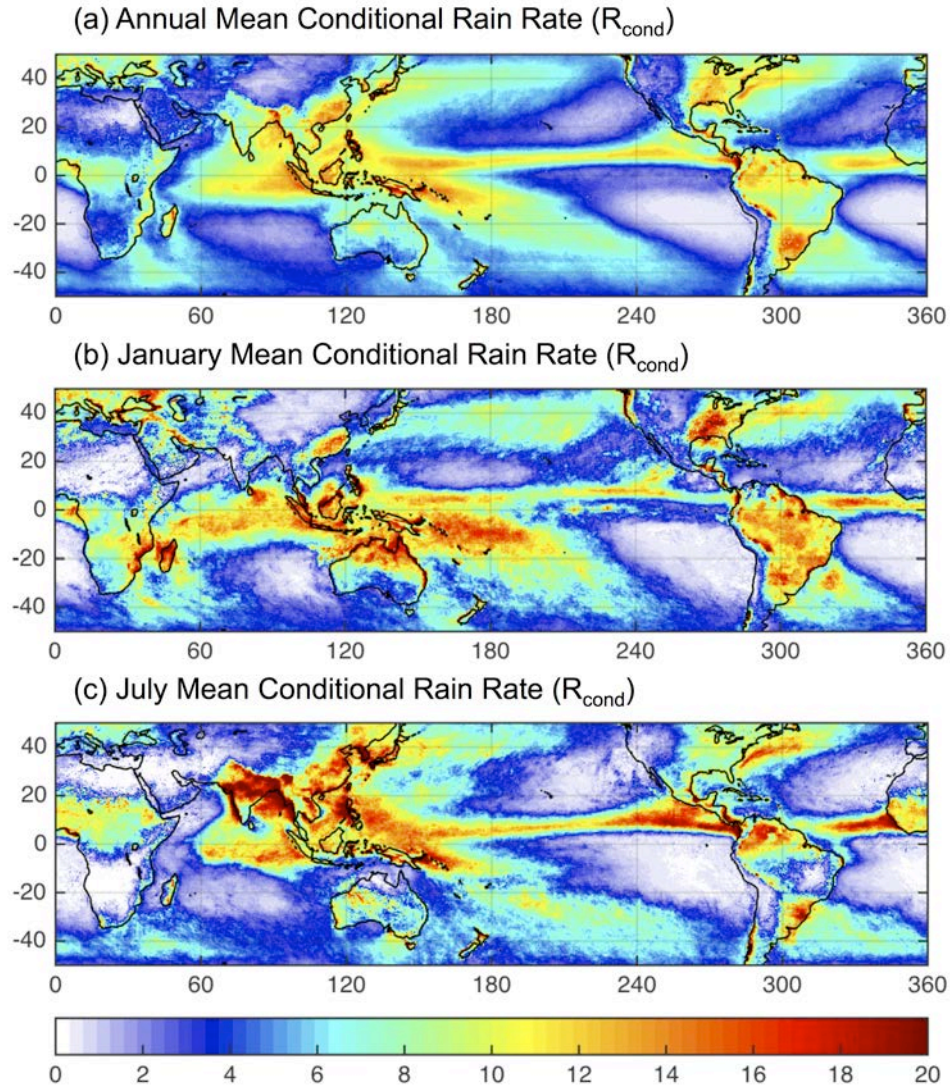
FIG. 3. (a) Annual, (b) January, and (c) July mean climatological conditional precipitation rate (R_{cond}, mm day^{-1}), derived from the TMPA 3B42 Version 7 data during 1998-2013.

(a) Annual Mean 95th Percentile (R_{95p})

(b) January Mean 95th Percentile (R_{95p})

(c) July Mean 95th Percentile (R_{95p})

981
982 **FIG. 4.** (a) Annual, (b) January, and (c) July mean 95th percentile daily precipitation
983 value (R_{95p}, mm day^{-1}), derived from the TMPA 3B42 Version 7 data during 1998-2013.

(a) Annual Mean Rain ≥ 95th Percentile (R95)

(b) January Mean Rain ≥ 95th Percentile (R95)

(c) July Mean Rain ≥ 95th Percentile (R95)

984
985 **FIG. 5.** (a) Annual, (b) January, and (c) July mean precipitation $\geq 95^{th}$ percentile daily
986 precipitation (R_{95}, mm day^{-1}), derived from the TMPA 3B42 Version 7 data during 1998-
987 2013.
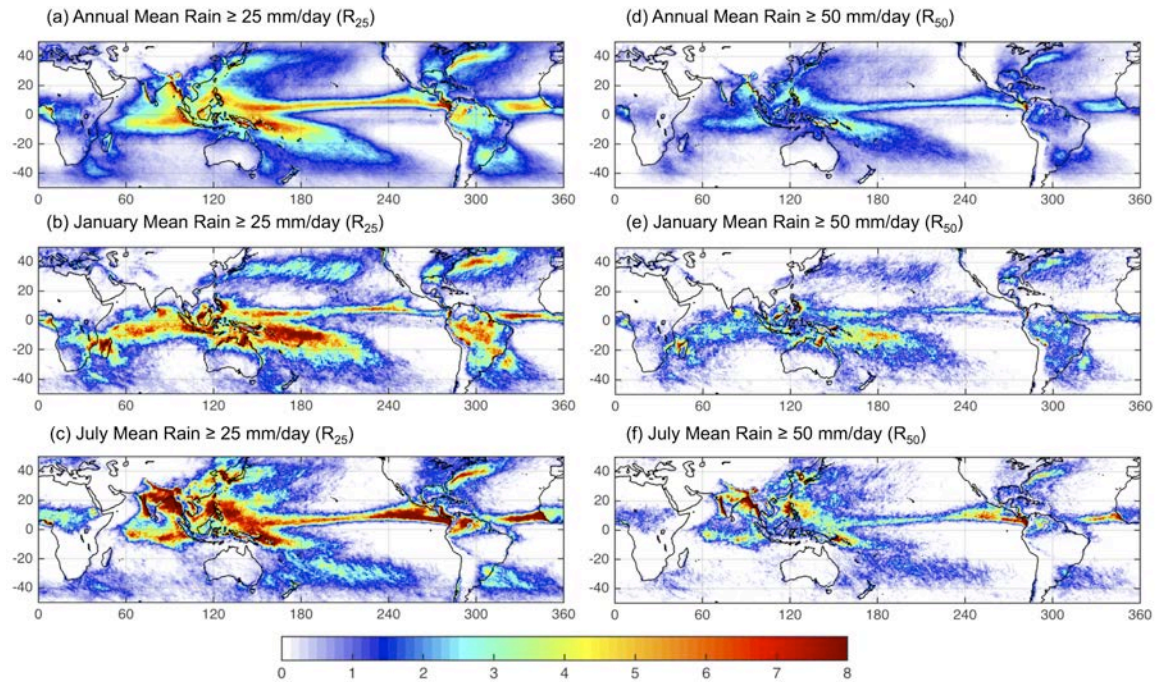
FIG. 6. Annual, January, and July mean precipitation (a)-(c) ≥ 25 mm day^{-1} threshold (R_{25}; mm day^{-1}) and (d)-(f) ≥ 50 mm day^{-1} threshold (R_{50}; mm day^{-1}), derived from the TMPA 3B42 Version 7 data during 1998-2013.

(a) Annual Mean Fraction of Rain ≥ 25 mm/day (F_{25})

(b) January Mean Fraction of Rain ≥ 25 mm/day (F_{25})

(c) July Mean Fraction of Rain ≥ 25 mm/day (F_{25})
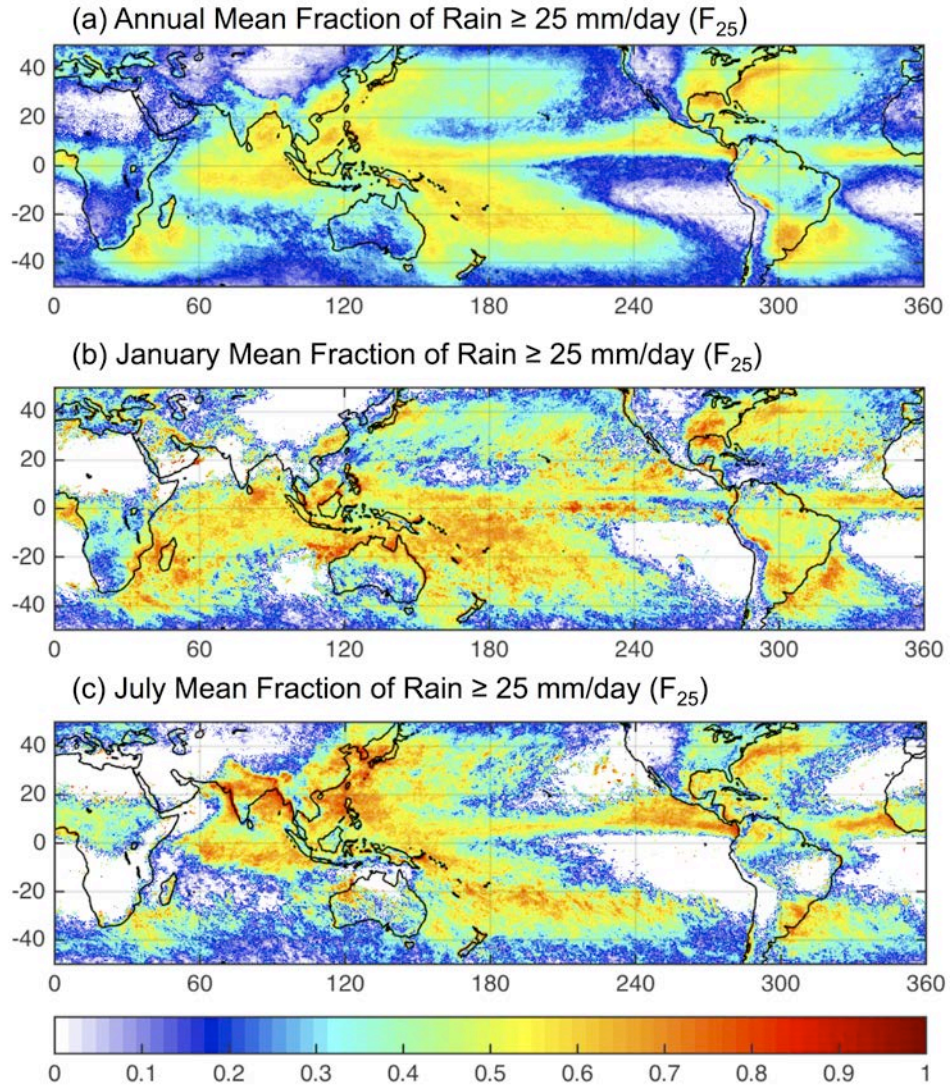
FIG. 7. (a) Annual, (b) January, and (c) July mean climatological fraction of daily precipitation ≥ 25 mm day^{-1} ($F_{25}=R_{25}/R_{mean}$), derived from the TMPA 3B42 Version 7 data during 1998-2013.
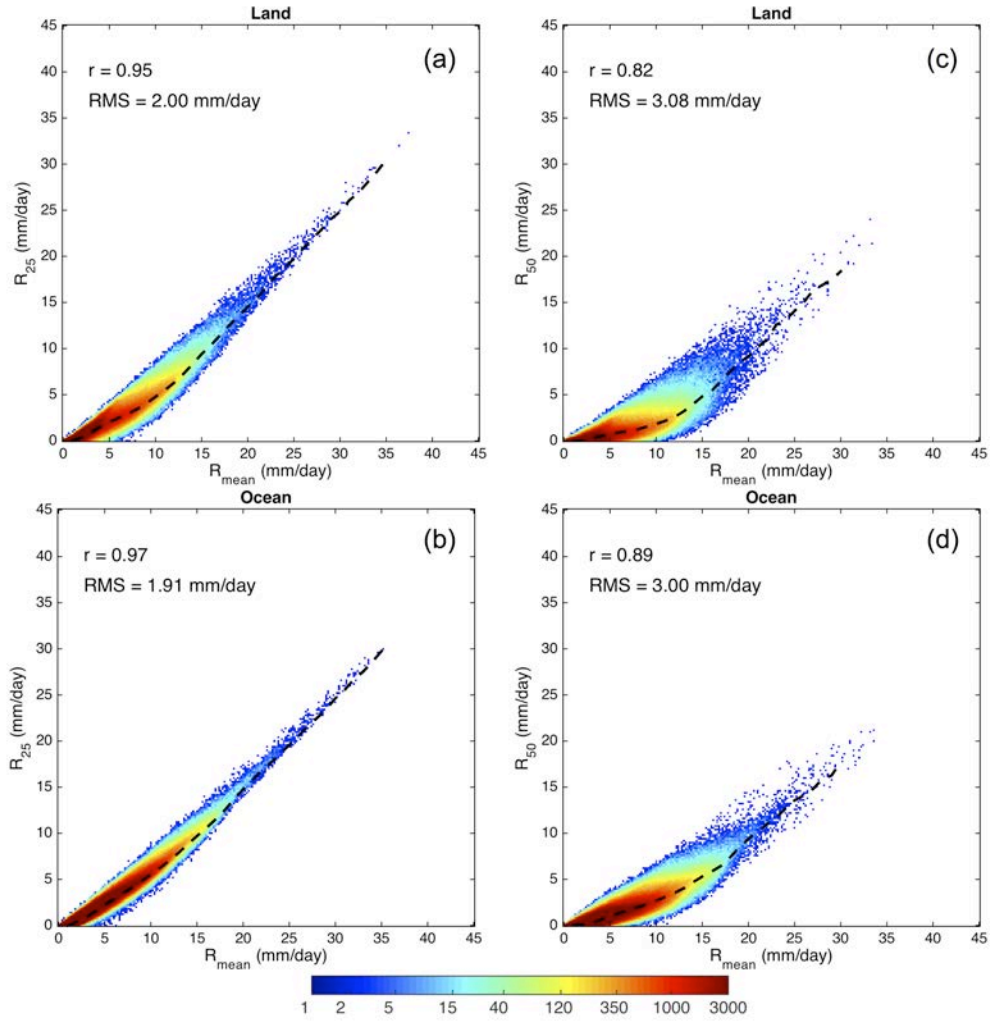
996
FIG. 8. Scatter plots of monthly climatology of mean precipitation (R_{mean}, mm day^{-1}) and
998 intense precipitation (a)-(b) ≥25 mm day^{-1} (R_{25}, mm day^{-1}) and (c)-(d) ≥50 mm day^{-1} (R_{50},
999 mm day^{-1}) over the TRMM domain (50°N-50°S), separately over land and ocean, derived
1000 from the TMPA 3B42 Version 7 data during 1998-2013. The color bar indicates the
1001 number of grid points with the attributed values in a logarithmic scale. Median (black
1002 dashed line) is calculated for a distribution of all 12 months. Correlation coefficient and
1003 RMS difference between intense rainfall (R_{25} and R_{50}) and R_{mean} are displayed.
1004 Correlation values are significant at the 95% confidence level.
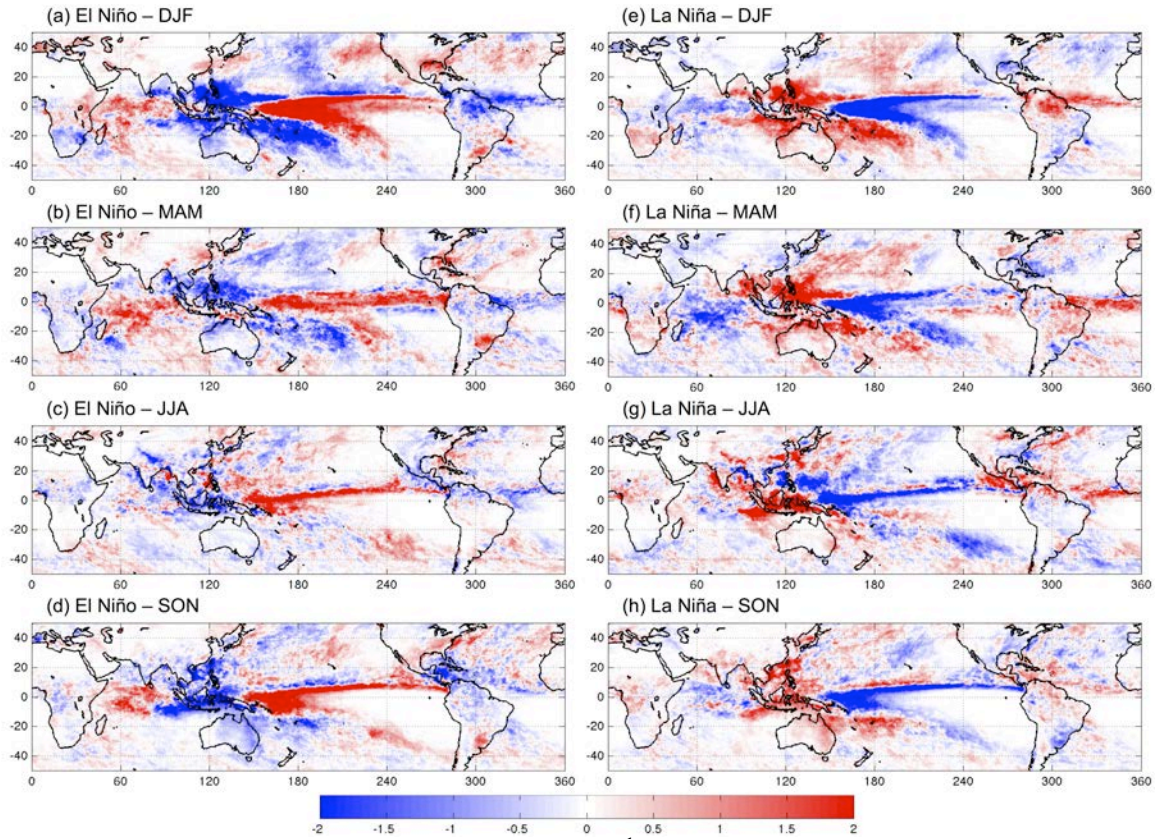
FIG. 9. Mean precipitation anomalies (mm day^{-1}) for 4 seasons (DJF, MAM, JJA, SON) for (a)-(d) El Niño and (e)-(h) La Niña period, derived from the TMPA 3B42 Version 7 data during 1998-2013.
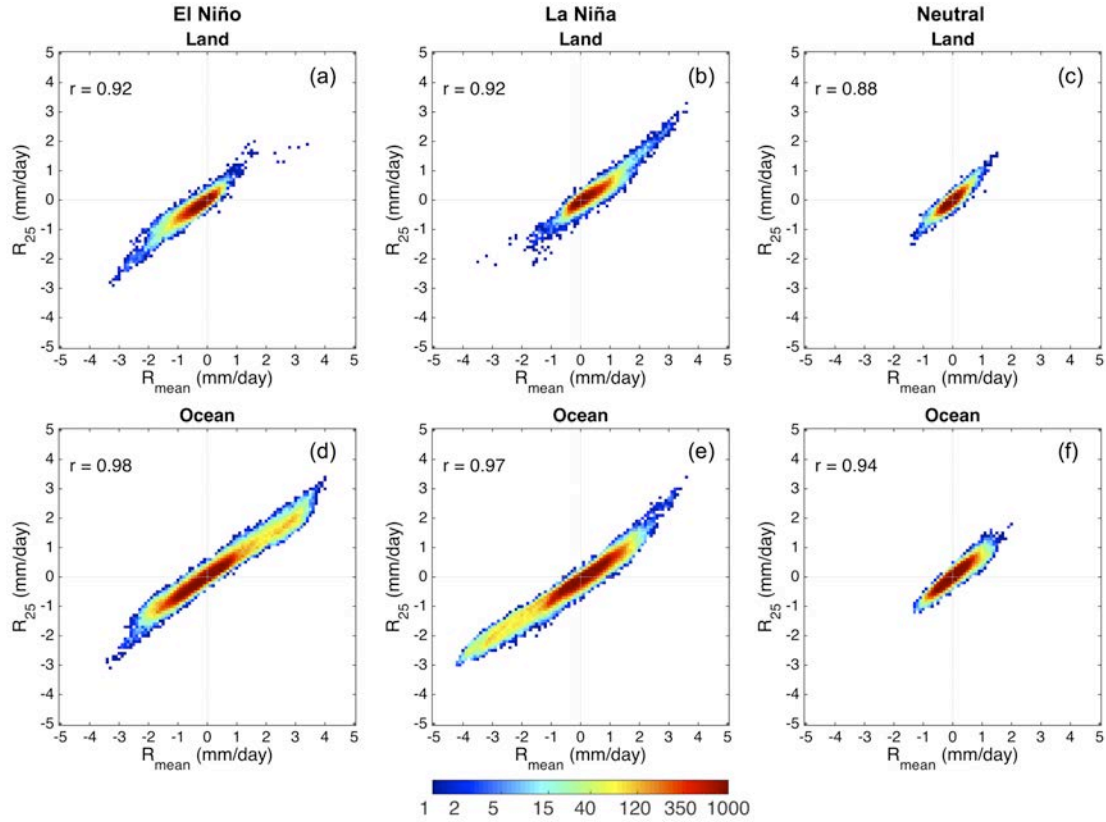
FIG. 10. Scatter plots of mean precipitation (R_{mean}, mm day^{-1}) and intense precipitation ≥25 mm day^{-1} (R_{25}, mm day^{-1}) anomalies for El Niño, La Niña and neutral period, over the tropical domain (23.5°N-23.5°S), over (a)-(c) land and (d)-(f) ocean, derived from the TMPA 3B42 Version 7 data during 1998-2013. The color bar indicates the number of grid points with the attributed values in a logarithmic scale. Correlation coefficient between R_{25} and R_{mean} is displayed. Correlation values are significant at the 95% confidence level.
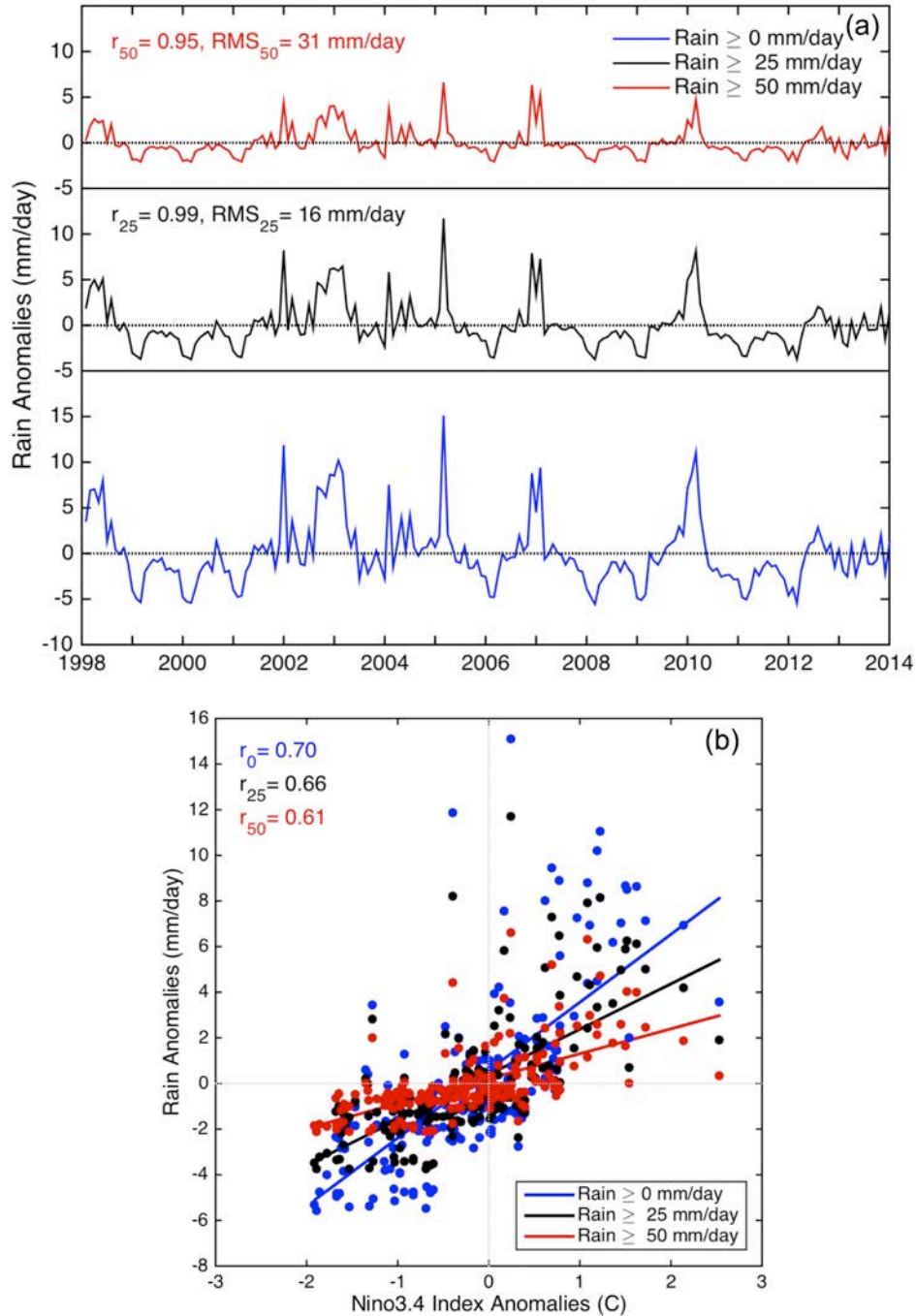
1017
FIG. 11. (a) Time series of mean precipitation (R_{mean}, mm day^{-1}; blue line) and intense
precipitation ≥25 mm day^{-1} (R_{25}, mm day^{-1}; black line) and ≥50 mm day^{-1} (R_{50}, mm day^{-1};
red line) anomalies, and (b) scatter plot of R_{mean}, R_{25}, and R_{50}, and Niño3.4 index
anomalies, averaged over a 5°x5° box over the West Pacific Ocean (6°S-1°S, 177°E-
182°E), derived from the TMPA 3B42 Version 7 precipitation data during 1998-2013.
Correlation coefficient and RMS difference between intense rainfall (R_{25} and R_{50}) and
R_{mean} are displayed in (a), and correlation coefficient between R_{mean}, R_{25}, and R_{50} with
respect to the Niño3.4 index in (b). Correlation values are significant at the 95%
confidence level.
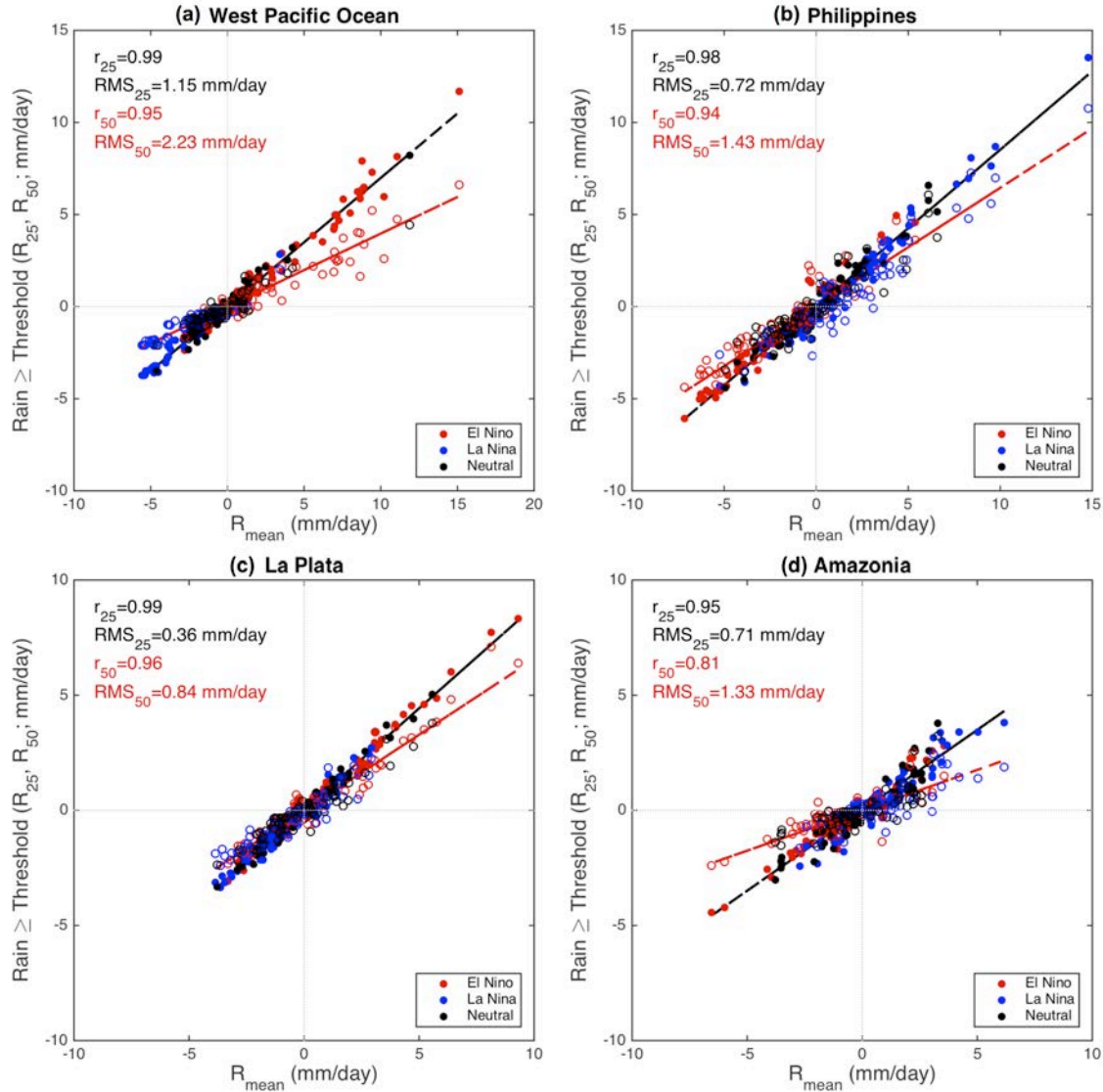
FIG. 12. Scatter plots of mean precipitation (R_{mean}; mm day^{-1}) and intense precipitation ≥ 25 mm day^{-1} (R_{25}, mm day^{-1}; filled circles and black line) and ≥ 50 mm day^{-1} (R_{50}, mm day^{-1}; empty circles and red line) anomalies, with corresponding linear fit for El Niño (red), La Niña (blue) and neutral period (black), averaged over a 5°x5° box over: (a) the West Pacific Ocean, (b) Philippines, (c) La Plata basin, and (d) Amazonia, derived from the TMPA 3B42 Version 7 data during 1998-2013. 5°x5° boxes are chosen denoting two largest maximums and minimums observed in global anomalies. Correlation coefficient and RMS difference between intense rainfall (R_{25} and R_{50}) and R_{mean} are displayed. Correlation values are significant at the 95% confidence level.